AIMS Mathematics

https://www.aimspress.com/journal/Math

AIMS Mathematics, 9(12): 35432–35470.
DOI: 10.3934/math.20241683
Received: 23 August 2024
Revised: 26 November 2024
Accepted: 29 November 2024
Published: 19 December 2024

Research article

Integrated ISPH approach with artificial neural network for magnetic influences on double diffusion of a non-Newtonian NEPCM in a curvilinear cavity

Weaam Alhejaili[1],*, Munirah Alotaibi[1] and Abdelraheem M. Aly[2]

[1] Department of Mathematical Sciences, College of Science, Princess Nourah bint Abdulrahman University, P.O. Box 84428, Riyadh 11671, Saudi Arabia
[2] Department of Mathematics, College of Science, King Khalid University, P.O. Box 9004, Abha 61413, Saudi Arabia

* **Correspondence:** Email: waalhejali@pnu.edu.sa; Tel: +966546669919.

Abstract: The artificial neural network (ANN) in conjunction with the incompressible smoothed particle hydrodynamics (ISPH) approach, deals with exothermic reaction effects on Cattaneo-Christov (Ca-Ch) heat and mass transport of nano-enhanced phase change material (NEPCM) in a curvilinear cavity. The ANN model, trained on data obtained from ISPH simulations, accurately predicted the mean $\overline{Nu}$ and $\overline{Sh}$ values. Two cases of boundary conditions included $(T_h \,\&\, C_h)$ on top/bottom walls and $(T_c \,\&\, C_c)$ on vertical walls and inner ellipse for C1. The boundary walls of a curvilinear cavity were kept at $(T_h \,\&\, C_h)$ and the inner ellipse was maintained at $(T_c \,\&\, C_c)$ for C2. The pertinent parameters were scaled as Frank-Kamenetskii number $Fk\,(0-1,)$ Ca–Ch heat, mass transfer parameters $(\delta_\theta \,\&\, \delta_\Phi)(0-0.2)$, Hartmann number $Ha(0-60)$, buoyancy ratio parameter $N(-2-4)$, power law index parameter $n\,(1.1-1.4)$, Rayleigh number $Ra\,(10^3-10^5)$, Soret/Dufour numbers $(Sr\&Du)(0-0.5)$, and fusion temperature $\theta_f(0.1-0.9)$. The simulation results demonstrated the effectiveness of Ca-Ch heat and mass transport parameters in lowering temperature and concentration within a curvilinear cavity at C1 and C2. Increasing $\delta_\theta \,\&\, \delta_\Phi$ from 0 to 0.2 resulted in a 44.1% and 48.9% drop in velocity field at C1 and C2, respectively. Boundary conditions (C1 and C2) significantly affected mass, heat transfer, heat capacity ratio, and velocity field within a curvilinear cavity. An increase in Power law index n from 1.1 to 1.4, reduced a velocity field by 64.68% and 64.66% at C1 and C2, respectively. Increasing Sr and Du helped distribute concentration. When Sr and Du were raised from 0 to 0.5, the velocity field increased by 34.17% and 29.73%, respectively, at C1 and C2.

Keywords: exothermic reaction; ANN model; ISPH method; Cattaneo-Christov; magnetic field
Mathematics Subject Classification: 76R10, 76M28, 35Q35, 68T07

Nomenclature

Acronym	Full name	Acronym	Full name
B_o	Strength of a magnetic field	C	Dimensional concentration
Cr	Heat capacity ratio	Du	Dufour number
D_1	Diffusion coefficient (m^2/s)	D_m	Mass diffusivity (m^2/s)
E	Activation energy parameter	k_s	Thermal conductivity (W/(m·K))
Fk	Frank-Kamenetskii number	Le	Lewis number
L	Length scale (m)	N	Buoyancy ratio parameter
n	Power-law index	g	Gravitational acceleration (m/s^2)
$\overline{Nu}$	Nusselt number (average)	P	Pressure (dimensionless)
MoD	Margin of deviation (%)	MLP	Multilayer perceptron
m	Total number of particles	ms	Mass of each particle
MSE	Mean squared error	R	Coefficient of determination
Ha	Hartmann number	Sr	Soret number
$\overline{Sh}$	Sherwood number (average)	Ra	Rayleigh number
Pr	Prandtl number	T	Temperature (K)
t	Time (s)	(U,V)	Velocities, dimensionless
(X,Y)	Cartesian coordinates, dimensionless	(x,y)	Cartesian coordinates, dimensional
α_f	Thermal diffusivity (m^2/s)	β_T	Thermal expansion coefficient (K^{-1})
ε	Non-dimensional porosity	β_C	Solutal expansion coefficient (K^{-1})
δ_T	Cattaneo heat transfer parameter (dimensional)	δ_C	Cattaneo mass transfer parameter (dimensional)
δ_θ	Cattaneo heat transfer parameter (dimensionless)	δ_Φ	Cattaneo mass transfer parameter (dimensionless)
Γ_b	Apparent viscosity (dimensional)	Π_b	Dimensionless apparent viscosity
Γ_{ref}	Reference viscosity	θ	Non-dimensional temperature
γ	Magnetic field angle	τ	Dimensionless time
σ	Electrical conductivity (S/m)	ϕ	Nanoparticle concentration
Φ	Dimensionless concentration	ρ	Density (kg/m^3)

1. Introduction

Contemporary computers can execute intricate numerical and symbolic calculations at an astonishingly rapid pace. However, they are far from matching the capabilities of human brains when it comes to carrying out perceptual tasks like language comprehension and image identification. Computers rely on accurate input data and sequentially execute instructions, but human brains carry out tasks through a distributed and parallel approach. The development of artificial intelligence that is modeled after biological neural networks results in the creation of an ANN. The ANNs are computational systems that were initially introduced by McCulloch and Pitts [1] and then by Metropolis et al. [2]. ANN models are most effective in situations where there is a substantial amount of experimental data available but no cohesive theoretical framework exists to establish prediction relationships. ANNs gained widespread usage in the 1980s due to substantial advancements in computing approaches that relied on self-organizing features and parallel information systems [3]. Lagaris et al. [4] employed artificial neural networks to address ordinary differential equations (ODEs) and partial differential equations (PDEs) in the context of both boundary value problems and initial value problems. Shafiq et al. [5] created an ANN model to forecast the flow of a nanofluid containing single-walled carbon nanotubes in the boundary layer. The flow is directed towards three distinct nonlinear thin needles with paraboloid, cone, and cylinder shapes. The needles are subjected to convective boundary conditions. The thermal conductivity model of the nanofluid considers the impact of both particle diameter and solid-fluid interface coating. The base fluid utilized in this model is ethylene glycol. Mitusch et al. [6] proposed a technique that integrates neural networks with physical principles expressed as PDEs. An ANN model was developed by Rehman et al. [7] to analyze the hydrodynamic force exerted on an object by numerous impediments during a flowing liquid stream. The ANN model was constructed using the multilayer perceptron (MLP), backpropagation (BP), and feed-forward (FF) network models. Sahu et al. [8] stressed the efficiency of the ANN model in analyzing velocity profiles in meandering flows. Aly et al. [9] employed the ISPH methodology in conjunction with machine learning (ML) to examine the influence of two different domain configurations, namely spline star and triangular star domains, on the double diffusion of NEPCM in the presence of heat radiation and exothermic chemical reactions. Gholami et al. [10] assessed the efficacy of computational fluid dynamics (CFD) and ANN models by comparing them to experimental data in the analysis of flow patterns in a steep 90-degree curve. Rackauckas et al. [11] suggest the incorporation of neural networks into finite difference schemes to enhance ODEs and PDEs. The findings indicate the potential for the advancement of hybrid PDE-NN models but do not exhibit the integration of more adaptable PDE discretization techniques like the FEM. Neural networks are highly effective methods for assessing the thermophysical properties of nanofluids, hence reducing the expenses and time required for conducting tests. Accurate computation of dynamic viscosity is crucial in heat transfer and nanofluid flow problems involving nanofluids. Motahar [12] investigated the rheological characteristics of a nanofluid phase change material that includes mesoporous silica nanoparticles. Ramezanizadeh et al. [13] conducted a review of machine learning methods employed in the moeling of a nanofluid viscosity. Ali et al. [14] documented the viscosity measurements of EG-water nanofluid and TiO_2 nanotubes within the temperature range of 25−65°C, mass fraction ranging from 0% to 1%, and shear stress ranging from 150 to 500 s-1. The viscosity was predicted using ANN and multivariable correlation approaches utilizing experimental data. The results indicate that the ANN technique achieved an accuracy of 0.1981 AAD% and 0.999 R2, demonstrating a high level of precision compared to the correlation method. A study conducted by Ahmadi et al. [15] utilized the ANN model to assess the dynamic viscosity of SiO2/EG-water nanofluid. A total of 160 experimental data points were utilized in their investigation. Their findings indicated that the ANN model effectively forecasted the dynamic viscosity of the nanofluid, with an MSE of 5.5 and a correlation coefficient of 0.998. The mesh-free approach is a promising tool for simulating astrophysical applications, free surface flows, and multi-phase flows. The SPH technique is a meshless method for dealing with these applications [16,17]. Hopp-Hirschler et al. [18] developed an SPH model to simulate thermo-capillary flows influenced by surface tension gradients, using a continuum surface force method that includes Marangoni effects. The model's accuracy was validated through convergence studies and comparisons with results from Open-FOAM and literature-based finite volume method (FVM) simulations. The work by Shadloo et al. [19] provided an in-depth review of the SPH method, highlighting its motivations, industrial applications, advantages in handling complex fluid flow scenarios, and the challenges that remain for its broader adoption in industrial settings. Cummins and Rudman [28] calculated the incompressibility factor using the SPH technique. Heat and mass transfer, as well as fluid movement in an enclosure, have attracted much attention due to their importance in engineering. Solar collectors, electrical appliances, and heat exchangers are only a few examples of applications [20,21]. Lewis et al. [22,23] explored the elementary numerical characteristics of heat transport, as well as fluid flow in porous media. PCMs were utilized to develop a new type of nanofluid known as NEPCMs. The natural convection of NEPCMs inside complex domains is explored in [24−30]. The review on thermal energy storage with phase change materials, heat transfer analysis, and applications is introduced by Zalba et al. [31]. The applications of PCM in thermal energy storage in buildings were investigated in references [32,33]. Giro-Paloma et al. [34] examined the progress of microencapsulated PCM in thermal energy storage (TES) systems, concentrating on the various encapsulation techniques and uses of these materials. Aly et al. [35] investigated how thermal radiation and magnetic influences affected the thermosolutal convection of NEPCMs in a wavy porous cavity including crescents. In the current work, ANN model with the ISPH technique is combined to investigate the effects of exothermic reactions on the Cattaneo-Christov (Ca-Ch) heat and mass transport behavior of NEPCM within a curvilinear cavity. This approach is motivated by the need for accurate modeling of non-Fourier heat conduction in complex industrial applications where precise temperature and concentration control are essential, such as in heat exchangers, advanced cooling systems, and thermal energy storage technologies. By focusing on non-Newtonian NEPCM influenced by magnetic fields, our findings have significant implications for improving the design and efficiency of systems dependent on rapid thermal response and stability. Moreover, the ANN-ISPH integration provides a novel predictive advantage in this context, supporting computational efficiency and accuracy for complex geometries and variable parameters. While the model presents several assumptions, including simplified boundary conditions, specific fluid properties, and the exclusion of viscous dissipation and thermal radiation, these factors are considered in interpreting the results and assessing their broader applicability to real-world scenarios.

2. Mathematical analysis

Figure 1 depicts the primary schematic diagram for the current physical challenge. A curvilinear cavity is suspended by non-Newtonian NEPCM, and it contains an inner ellipse. Two cases of boundary conditions are conducted with C1, $(T_h \,\&\, C_h)$ on the top/bottom walls, and $(T_c \,\&\, C_c)$ on the side walls. C2 has $(T_h \,\&\, C_h)$ on the boundary walls and $(T_c \,\&\, C_c)$ on the ellipse. The base fluid is a non-Newtonian fluid that is suspended using NEPCM. We do not consider viscous dissipation or thermal radiation.

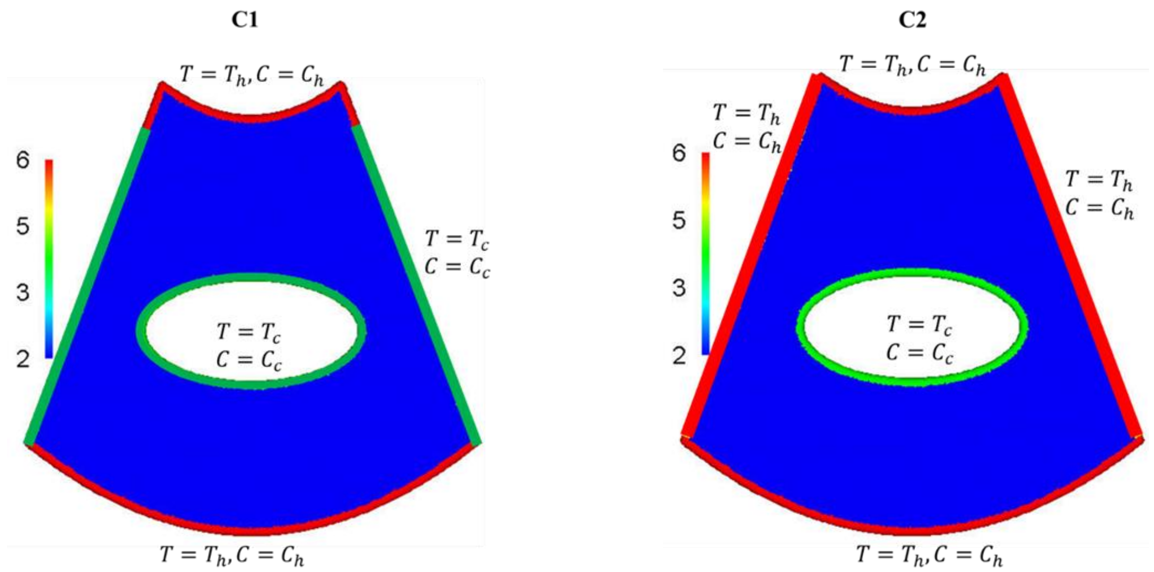

Figure 1. A primary schematic diagram.

The dimensional governing equations in the Lagrangian description are:

$$\frac{\partial u}{\partial x} + \frac{\partial v}{\partial y} = 0, \tag{1}$$

$$\rho_b \frac{Du}{Dt} = -\frac{\partial p}{\partial x} + \left(\frac{\partial \tau_{xx}}{\partial \mathrm{x}} + \frac{\partial \tau_{yx}}{\partial y}\right) - B_o^2\, \delta_b (u\, sin^2\gamma - v\, sin\gamma\, cos\gamma), \tag{2}$$

$$\begin{aligned}\rho_b \frac{Dv}{Dt} = -\frac{\partial p}{\partial y} + \left(\frac{\partial \tau_{xy}}{\partial \mathrm{x}} + \frac{\partial \tau_{yy}}{\partial y}\right) + (\rho\beta_T)_b g(T - T_c) + (\rho\beta_T)_b\, \mathrm{g}(C - C_c) \\ - B_o^2\, \delta_b (v\, cos^2\gamma - u\, sin\gamma\, cos\gamma),\end{aligned} \tag{3}$$

$$\begin{aligned}(\rho C)_b \frac{DT}{Dt} = k_b \left(\frac{\partial^2 T}{\partial x^2} + \frac{\partial^2 T}{\partial y^2}\right) + D_1 \left(\frac{\partial^2 C}{\partial x^2} + \frac{\partial^2 C}{\partial y^2}\right) + \frac{1}{(\rho C_P)_{\mathrm{nf}}} \frac{Q k_o a}{e^{\frac{E}{RT}}} \\ - \delta_T \left(u \frac{\partial T}{\partial x}\frac{\partial u}{\partial x} + v \frac{\partial T}{\partial y}\frac{\partial v}{\partial y} + u^2 \frac{\partial^2 T}{\partial x^2} + v^2 \frac{\partial^2 T}{\partial y^2} + 2uv \frac{\partial^2 T}{\partial x \partial y} + u \frac{\partial T}{\partial y}\frac{\partial v}{\partial x} \right. \\ \left. + v \frac{\partial T}{\partial x}\frac{\partial u}{\partial y}\right),\end{aligned} \tag{4}$$

$$\begin{aligned}\frac{DC}{Dt} = \nabla \cdot (D_2\, \nabla T) + \nabla \cdot (D_m\, \nabla C) \\ - \delta_C \left(u \frac{\partial C}{\partial x}\frac{\partial u}{\partial x} + v \frac{\partial C}{\partial y}\frac{\partial v}{\partial y} + u^2 \frac{\partial^2 C}{\partial x^2} + v^2 \frac{\partial^2 C}{\partial y^2} + 2uv \frac{\partial^2 C}{\partial x \partial y} + u \frac{\partial C}{\partial y}\frac{\partial v}{\partial x} \right. \\ \left. + v \frac{\partial C}{\partial x}\frac{\partial u}{\partial y}\right).\end{aligned} \tag{5}$$

Here, τ indicates shear stress tensor. The power-law scheme can be applied to define τ as follows [36,37]:

$$\tau_{ij} = \Gamma_b \left(\frac{\partial u_i}{\partial \mathrm{x}_j} + \frac{\partial u_j}{\partial x_i}\right), \tag{6}$$

$$\Gamma_b = \mu_b \left(2\left(\frac{\partial u}{\partial x}\right)^2 + 2\left(\frac{\partial v}{\partial y}\right)^2 + \left(\frac{\partial u}{\partial y} + \frac{\partial v}{\partial x}\right)^2\right)^{\frac{n-1}{2}}, \tag{7}$$

where Γ_b, n, and μ_b illustrate apparent viscosity, power-law index, and consistency index, respectively.

The mixture's density is:

$$\rho_b = \varphi\rho_p + \rho_f - \varphi\rho_f, \tag{8}$$

ρ_p is provided by:

$$\rho_p = \frac{(1+\chi)\rho_s\,\rho_c}{\rho_s + \chi\,\rho_c}. \tag{9}$$

The dynamic viscosity, thermal conductivity, and thermal expansion are as follows:

$$\mu_b = \mu_f(1 + N_1\varphi), k_b = k_f(1 + N_2\varphi), \beta_b = \beta_f - \varphi\beta_f + \varphi\beta_p. \tag{10}$$

The specific heat capacity ratio is:

$$(C_p)_b = \frac{\varphi\rho_p(C_p)_p + \rho_f(C_p)_f - \varphi\rho_f(C_p)_f}{\rho_b}. \tag{11}$$

The heat capacity ratio of NEPCM:

$$(C_p)_p = \frac{((C_p)_{c,l} + \chi(C_p)_s)\rho_s\,\rho_c}{(\rho_s + \chi\,\rho_c)\rho_p}. \tag{12}$$

The rectangular, triangular, or sine profiles are:

$$(C_p)_c = (C_p)_{c,l} + \frac{h_{sf}}{T_{Mr}} \tag{13}$$

$$(C_p)_c = (C_p)_{c,l} + 2\left(\frac{h_{sf}}{T_{Mr}^2} - \frac{(C_p)_{c,l}}{T_{Mr}}\right)(T - T_1) \tag{14}$$

$$(C_p)_c = (C_p)_{c,l} + \left[\frac{\pi}{2}\left(\frac{h_{sf}}{T_{Mr}} - (C_p)_{c,l}\right)\sin\left(\pi\frac{T - T_f + \frac{T_{Mr}}{2}}{T_{Mr}}\right)\right]\omega \tag{15}$$

where

$$\omega = \begin{cases} 0 & T < T_f - \dfrac{T_{Mr}}{2} \\ 1 & \left(T_f - \dfrac{T_{Mr}}{2}\right) < T < \left(T_f + \dfrac{T_{Mr}}{2}\right). \\ 0 & T > T_f + \dfrac{T_{Mr}}{2} \end{cases} \tag{16}$$

The sine profile was employed in this investigation. The dimensionless amounts are:

$$\tau = \frac{t\alpha_f}{L^2}, X = \frac{x}{L}, Y = \frac{y}{L}, U = \frac{uL}{\alpha_f}, V = \frac{vL}{\alpha_f}, \Phi = \frac{C - C_c}{C_h - C_c}, P = \frac{pL^2}{\rho_f\alpha_f^2}, \theta = \frac{T - T_c}{T_h - T_c}. \tag{17}$$

After incorporating dimensionless quantities (Eq (17)) to Eqs (1)−(5), the dimensionless equations that regulate a physical issue according to the Lagrangian description are:

$$\frac{\partial U}{\partial X} = -\frac{\partial V}{\partial Y}, \tag{18}$$

$$\begin{aligned} &\frac{DU}{D\tau} + \frac{\sigma_b}{\sigma_f}\frac{\rho_f}{\rho_b}Pr\,Ha^2(U\,sin^2\gamma - V\,sin\gamma\,cos\gamma) \\ &= -\frac{\rho_f}{\rho_b}\frac{\partial P}{\partial X} + \frac{\mu_b}{\mu_f}\frac{\rho_f}{\rho_b}Pr\left(\frac{\partial}{\partial X}\left(2\Pi_b\frac{\partial U}{\partial X}\right) + \frac{\partial}{\partial Y}\left(\Pi_b\left(\frac{\partial V}{\partial X} + \frac{\partial U}{\partial Y}\right)\right)\right), \end{aligned} \tag{19}$$

$$\frac{DV}{D\tau}+\frac{\sigma_b}{\sigma_f}\frac{\rho_f}{\rho_b}Pr\,Ha^2(V\cos^2\gamma\ -U\sin\gamma\cos\gamma)$$
$$=-\frac{\rho_f}{\rho_b}\frac{\partial P}{\partial Y}+\frac{\mu_b}{\mu_f}\frac{\rho_f}{\rho_b}Pr\left(\frac{\partial}{\partial Y}\left(2\Pi_b\frac{\partial V}{\partial Y}\right)+\frac{\partial}{\partial X}\left(\Pi_b\left(\frac{\partial V}{\partial X}+\frac{\partial U}{\partial Y}\right)\right)\right) \tag{20}$$
$$+\frac{(\rho\beta)_b}{(\rho\beta)_f}\frac{\rho_f}{\rho_b}Ra\,Pr(\theta+N\Phi),$$

$$Cr\frac{D\theta}{D\tau}=\frac{k_b}{k_f}\left(\frac{\partial^2\theta}{\partial X^2}+\frac{\partial^2\theta}{\partial Y^2}\right)+Du\left(\frac{\partial^2\Phi}{\partial X^2}+\frac{\partial^2\Phi}{\partial Y^2}\right)+Fk\,e^{\theta}$$
$$-\delta_\theta\left(U\frac{\partial\theta}{\partial X}\frac{\partial U}{\partial X}+V\frac{\partial\theta}{\partial Y}\frac{\partial V}{\partial Y}+U^2\frac{\partial^2\theta}{\partial X^2}+V^2\frac{\partial^2\theta}{\partial Y^2}+2UV\frac{\partial^2\theta}{\partial X\partial Y}+U\frac{\partial\theta}{\partial Y}\frac{\partial V}{\partial X}\right. \tag{21}$$
$$\left.+V\frac{\partial\theta}{\partial X}\frac{\partial U}{\partial Y}\right),$$

$$\frac{D\Phi}{D\tau}=\frac{1}{Le}\left(\frac{\partial^2\Phi}{\partial X^2}+\frac{\partial^2\Phi}{\partial Y^2}\right)+\ Sr\left(\frac{\partial^2\theta}{\partial X^2}+\frac{\partial^2\theta}{\partial Y^2}\right)$$
$$-\delta_\Phi\left(U\frac{\partial\Phi}{\partial X}\frac{\partial U}{\partial X}+V\frac{\partial\Phi}{\partial Y}\frac{\partial V}{\partial Y}+U^2\frac{\partial^2\Phi}{\partial X^2}+V^2\frac{\partial^2\Phi}{\partial Y^2}+2UV\frac{\partial^2\Phi}{\partial X\partial Y}+U\frac{\partial\Phi}{\partial Y}\frac{\partial V}{\partial X}\right. \tag{22}$$
$$\left.+V\frac{\partial\Phi}{\partial X}\frac{\partial U}{\partial Y}\right).$$

where,

$$\Pi_b=\left(2\left(\frac{\partial U}{\partial X}\right)^2+2\left(\frac{\partial V}{\partial Y}\right)^2+\left(\frac{\partial U}{\partial Y}+\frac{\partial V}{\partial X}\right)^2\right)^{\frac{n-1}{2}}. \tag{23}$$

The dimensionless boundary conditions:

$$\begin{array}{ll} \textbf{C1} & \text{Top/bottom walls: } U=0=V,\theta=1=\Phi, \\ & \text{Inner ellipse and vertical walls: } U=0=V,\theta=0=\Phi, \\ \textbf{C2} & \text{Top/bottom and vertical walls: } U=0=V,\theta=1=\Phi, \\ & \text{Inner ellipse: } U=0=V,\theta=0=\Phi. \end{array} \tag{24}$$

The heat capacity ratio:

$$Cr=\varphi(\lambda-1)+\frac{\varphi}{\delta Ste}\left[\frac{\pi}{2}\Gamma\sin\left(\frac{\pi}{\delta}(\theta-\theta_f+\frac{\delta}{2}\right)\right]+1, \tag{25}$$

with

$$\Gamma=\begin{cases}0 & \theta<\theta_f-\frac{\delta}{2}\\ 1 & \left(\theta_f-\frac{\delta}{2}\right)<\theta<\left(\theta_f+\frac{\delta}{2}\right),\\ 0 & \theta>\theta_f+\frac{\delta}{2}\end{cases} \tag{26}$$

where, $Ste=\frac{(\rho C_p)_f\Delta T(\rho_s+\chi\,\rho_c)}{(1+\chi)h_{sf}\rho_s\,\rho_c}$, $\lambda=\frac{((C_p)_{c,l}+\chi(C_p)_s)\rho_s\,\rho_c}{(\rho_s+\chi\,\rho_c)(\rho C_p)_f}$, $\theta_f=\frac{T_f-T_c}{\Delta T}$, $\delta=\frac{T_{Mr}}{\Delta T}$.

The Sherwood and Nusselt average numbers are:

$$\overline{Sh}\ =\ \frac{-1}{L_h}\int_0^{L_h}\frac{\partial\Phi}{\partial\boldsymbol{n}}\,d\zeta, \tag{27}$$

$$\overline{Nu}\ =\ \frac{-1}{L_h}\int_0^{L_h}\frac{k_{m,b}}{k_f}\frac{\partial\theta}{\partial\boldsymbol{n}}\,d\zeta, \tag{28}$$

3. Numerical method

3.1. The SPH formulation

The core idea behind SPH representation for any function is:

$$f(\boldsymbol{X}_i) = \sum_{j=1}^{m} \frac{ms_j}{\rho_j} f(\boldsymbol{X}_j) W(\boldsymbol{r}_{ij}, h), \tag{29}$$

$$W(q,h) = \frac{7}{478\,\pi\,h^2} \begin{cases} (3-q)^5 - 6(2-q)^5 + 15(1-q)^5, & 0 \le q < 1 \\ (3-q)^5 - 6(2-q)^5, & 1 \le q < 2 \\ (3-q)^5, & 2 \le q < 3 \\ 0, & q \ge 3 \end{cases}. \tag{30}$$

Here, W is a kernel function.

The modified first derivative in the SPH method, as referenced in [38], is:

$$\widetilde{\nabla} W_{ij} = \boldsymbol{L}(\boldsymbol{r}_{ij}) \nabla W_{ij}, \tag{31}$$

where

$$\boldsymbol{L}(\boldsymbol{r}_{ij}) = \begin{pmatrix} \sum_{j=1}^{m} \frac{ms_j}{\rho_j} (X_j - X_i) \frac{\partial W_{ij}}{\partial X_i} & \sum_{j=1}^{m} \frac{ms_j}{\rho_j} (X_j - X_i) \frac{\partial W_{ij}}{\partial Y_i} \\ \sum_{j=1}^{m} \frac{ms_j}{\rho_j} (Y_j - Y_i) \frac{\partial W_{ij}}{\partial X_i} & \sum_{j=1}^{m} \frac{ms_j}{\rho_j} (Y_j - Y_i) \frac{\partial W_{ij}}{\partial Y_i} \end{pmatrix}^{-1}. \tag{32}$$

The expressions for the velocity divergence, pressure gradient, and the second derivative approximation are outlined below:

$$\nabla \cdot \mathbf{U}(\boldsymbol{X}_i) = \sum_{j=1}^{m} \frac{ms_j}{\rho_j} \left(\mathbf{U}(\boldsymbol{X}_j) - \mathbf{U}(\boldsymbol{X}_i) \right) \cdot \widetilde{\nabla} W_{ij}, \tag{33}$$

$$\nabla P(\boldsymbol{X}_i) = \rho_i \sum_{j=1}^{m} ms_j \left(\frac{P_i}{\rho_i^2} + \frac{P_j}{\rho_j^2} \right) \nabla W_{ij}, \tag{34}$$

$$\nabla^2 f(\boldsymbol{X}_i) = \sum_{j=1}^{m} ms_j \left(\frac{\rho_i + \rho_j}{\rho_i \rho_j} \frac{(\boldsymbol{r}_i - \boldsymbol{r}_j) \cdot \nabla_i W_{ij}}{r_{ij}^2 + 0.0001\,h^2} \right) \left(f(\boldsymbol{X}_j) - f(\boldsymbol{X}_i) \right). \tag{35}$$

In SPH, dummy wall particles (as shown in Figure 2) are used to enforce boundary conditions by preventing fluid penetration and ensuring correct interaction with the boundary. They replicate solid surfaces, aiding in stable pressure distribution and accurate momentum transfer.

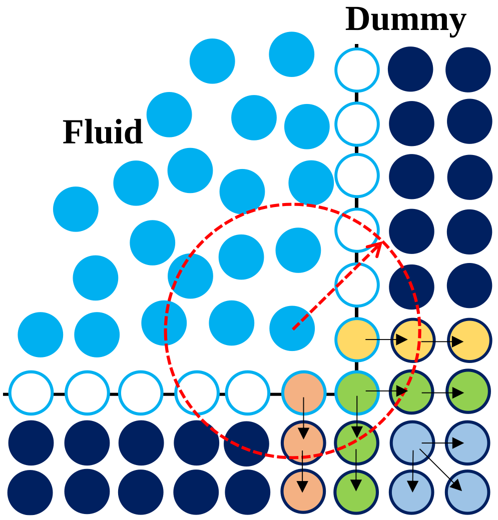

Figure 2. Sketch for dummy wall boundary particles.

3.2. The ISPH method

The solving steps of the present ISPH scheme are:
Predicted velocities:

$$U^* = U^m + \Delta\tau\left(-\frac{\sigma_b}{\sigma_f}\frac{\rho_f}{\rho_b}Pr\, Ha^2(U\, sin^2\gamma - V\, sin\gamma\, cos\gamma)^m\right.$$
$$\left.+\frac{\mu_b}{\mu_f}\frac{\rho_f}{\rho_b}Pr\left(\frac{\partial}{\partial X}\left(2\Pi_b\frac{\partial U}{\partial X}\right)+\frac{\partial}{\partial Y}\left(\Pi_b\left(\frac{\partial V}{\partial X}+\frac{\partial U}{\partial Y}\right)\right)\right)^m\right), \tag{36}$$

$$V^* = V^m + \Delta\tau\left(-\frac{\sigma_b}{\sigma_f}\frac{\rho_f}{\rho_b}Pr\, Ha^2(V\, cos^2\gamma - U\, sin\gamma\, cos\gamma)^m\right.$$
$$+\frac{\mu_b}{\mu_f}\frac{\rho_f}{\rho_b}Pr\left(\frac{\partial}{\partial Y}\left(2\Pi_b\frac{\partial V}{\partial Y}\right)+\frac{\partial}{\partial X}\left(\Pi_b\left(\frac{\partial V}{\partial X}+\frac{\partial U}{\partial Y}\right)\right)\right)^m \tag{37}$$
$$\left.+\frac{(\rho\beta)_b}{(\rho\beta)_f}\frac{\rho_f}{\rho_b}Ra\, Pr(\theta + N\Phi)^m\right).$$

Solving the pressure Poisson equation:

$$\nabla^2 P^{m+1} = \frac{1}{\Delta\tau}\frac{\rho_b}{\rho_f}\left(\frac{\partial U^*}{\partial X}+\frac{\partial V^*}{\partial Y}\right) + \Upsilon\frac{(\rho_f - \rho^{num})}{\rho_f\,\Delta\tau^2}. \tag{38}$$

Υ represents a relaxation coefficient.
Velocity corrections:

$$U^{m+1} = U^* - \Delta\tau\,\frac{\rho_f}{\rho_b}\left(\frac{\partial P}{\partial X}\right)^{m+1}, \tag{39}$$

$$V^{m+1} = V^{*} - \varDelta\tau \, \frac{\rho_f}{\rho_b}\left(\frac{\partial P}{\partial Y}\right)^{m+1}. \tag{40}$$

Thermal and concentration are updated as:

$$\begin{aligned}\theta^{m+1} = {} & \theta^{m} + \frac{\varDelta\tau}{Cr}\left(\frac{k_b}{k_f}\left(\frac{\partial^2\theta}{\partial X^2} + \frac{\partial^2\theta}{\partial Y^2}\right)^{m} + Du\left(\frac{\partial^2\Phi}{\partial X^2} + \frac{\partial^2\Phi}{\partial Y^2}\right)^{m} + Fk\left(e^{\theta}\right)^{m}\right. \\ & - \delta_\theta\left(U\frac{\partial\theta}{\partial X}\frac{\partial U}{\partial X} + V\frac{\partial\theta}{\partial Y}\frac{\partial V}{\partial Y} + U^2\frac{\partial^2\theta}{\partial X^2} + V^2\frac{\partial^2\theta}{\partial Y^2} + 2UV\frac{\partial^2\theta}{\partial X\partial Y} + U\frac{\partial\theta}{\partial Y}\frac{\partial V}{\partial X}\right. \\ & \left.\left. + V\frac{\partial\theta}{\partial X}\frac{\partial U}{\partial Y}\right)^{m}\right),\end{aligned} \tag{41}$$

$$\begin{aligned}\Phi^{m+1} = {} & \Phi^{m} + \varDelta\tau\left(\frac{1}{Le}\left(\frac{\partial^2\Phi}{\partial X^2} + \frac{\partial^2\Phi}{\partial Y^2}\right)^{m} + Sr\left(\frac{\partial^2\theta}{\partial X^2} + \frac{\partial^2\theta}{\partial Y^2}\right)^{m}\right. \\ & - \delta_\Phi\left(U\frac{\partial\Phi}{\partial X}\frac{\partial U}{\partial X} + V\frac{\partial\Phi}{\partial Y}\frac{\partial V}{\partial Y} + U^2\frac{\partial^2\Phi}{\partial X^2} + V^2\frac{\partial^2\Phi}{\partial Y^2} + 2UV\frac{\partial^2\Phi}{\partial X\partial Y} + U\frac{\partial\Phi}{\partial Y}\frac{\partial V}{\partial X}\right. \\ & \left.\left. + V\frac{\partial\Phi}{\partial X}\frac{\partial U}{\partial Y}\right)^{m}\right).\end{aligned} \tag{42}$$

The updated positions are:

$$X^{m+1} = X^{m} + \varDelta\tau \; U^{m+1}, \tag{43}$$

$$Y^{m+1} = Y^{m} + \varDelta\tau \, V^{m+1}. \tag{44}$$

The shifting strategy is:

$$\mathcal{F}_{i'} = -(\nabla\mathcal{F})_i \cdot (\mathcal{D}\,\nabla C'_i) + \mathcal{F}_i + \mathcal{O}\left(\delta \boldsymbol{r}_{ii'}^2\right). \tag{45}$$

4. Validation tests

In this section, a mesh independence test is conducted as a preliminary step to ensure the numerical accuracy and stability of the ISPH method, followed by several numerical and experimental tests to demonstrate the efficiency and reliability of the present scheme. Table 1 demonstrates the mesh independence test results for various particle sizes, d_0, ranging from 0.02 to 0.0025. The test evaluates the average Nusselt number ($\overline{Nu}$) and Sherwood number ($\overline{Sh}$) for both cases. As the particle size decreases, the results stabilize, indicating mesh independence. The particle size $d_0 = 0.01$ is selected as the suitable choice, balancing accuracy and computational cost effectively.

Table 1. Mesh independence test results for two cases of boundary conditions (C1 and C2).

Particle size (d_o)	$C1$		$C2$		**Suitable Choice**
	$\overline{Nu}$	$\overline{Sh}$	$\overline{Nu}$	$\overline{Sh}$	
0.02	1.54012	1.14015	1.05011	1.47022	No
0.015	1.56489	1.14508	1.07023	1.47514	No
0.01	1.57491	1.14902	1.08067	1.47813	Yes
0.005	1.57502	1.14915	1.081	1.47845	No
0.0025	1.57499	1.14925	1.08105	1.4786	No

For validation, three distinct numerical and experimental comparisons are presented to evaluate the performance of the ISPH method. These comparisons include finite element method (FEM) results, prior SPH models, and experimental data, ensuring a robust assessment of the method's accuracy and reliability. The current study incorporates refinement in particle resolution, specifically at $d_0 = 0.015$ and $d_0 = 0.01$, to address discrepancies and improve alignment with FEM results. Such refinements demonstrate the ISPH method's ability to replicate established numerical outcomes and experimental observations effectively, emphasizing its robustness across a wide range of thermal and fluid dynamic conditions. Figure 3 compares the average Nusselt number ($\overline{Nu}$) obtained using the ISPH and FEM methods across varying Rayleigh numbers. The solid black line represents FEM results, while the blue and red markers indicate ISPH outcomes at $d_0 = 0.015$ and $d_0 = 0.01$, respectively. Both methods show an increase in $\overline{Nu}$ with higher Rayleigh numbers, reflecting enhanced convective heat transfer. The close agreement between ISPH and FEM results validates the accuracy of the ISPH method for natural convection simulations. Minor deviations may be attributed to differences in numerical approaches, particle discretization, and resolution effects. Figure 4 illustrates the temperature profiles (θ) along the X-axis as obtained using FEM, ISPH, and SPH methods. The refined ISPH profiles align closely with FEM benchmarks and prior SPH results from Hopp-Hirschler et al. [18], validating the accuracy of ISPH in capturing detailed temperature fields. This comparison highlights the suitability of ISPH for scenarios requiring precise thermal analysis, with improvements due to refined particle resolution. Figure 5 illustrates a comparative analysis of isotherm patterns generated using the ISPH method alongside numerical and experimental results from Paroncini and Corvaro [39]. The top row corresponds to a lower Rayleigh number $Ra = 1.02 \times 10^5$ with a heater height $\zeta = 0.25$ showing how thermal gradients distribute under moderate convective conditions. The ISPH method replicates the isotherm structures seen in both numerical and experimental results, indicating consistency in capturing temperature fields. The bottom row presents results at a higher Rayleigh number $Ra = 2.25 \times 10^5$ and $\zeta = 0.5$ where stronger convection leads to more pronounced and complex isotherm patterns. The close agreement among all three approaches underscores the reliability of the ISPH method in simulating convective heat transfer, aligning well with established numerical data and physical experiments.

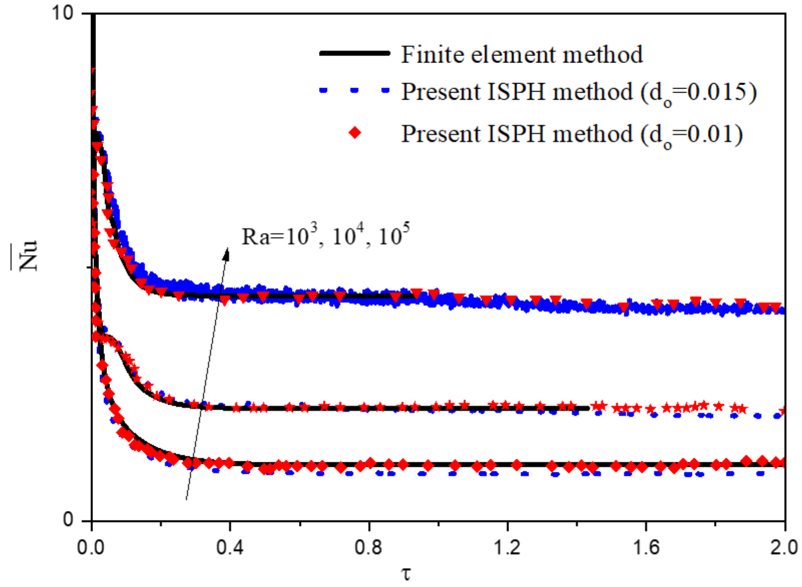

Figure 3. Comparison of the average Nusselt number ($\overline{Nu}$) at different Rayleigh numbers obtained using the present ISPH method at two particle resolutions ($d_0 = 0.015$ and $d_0 = 0.01$) and FEM.

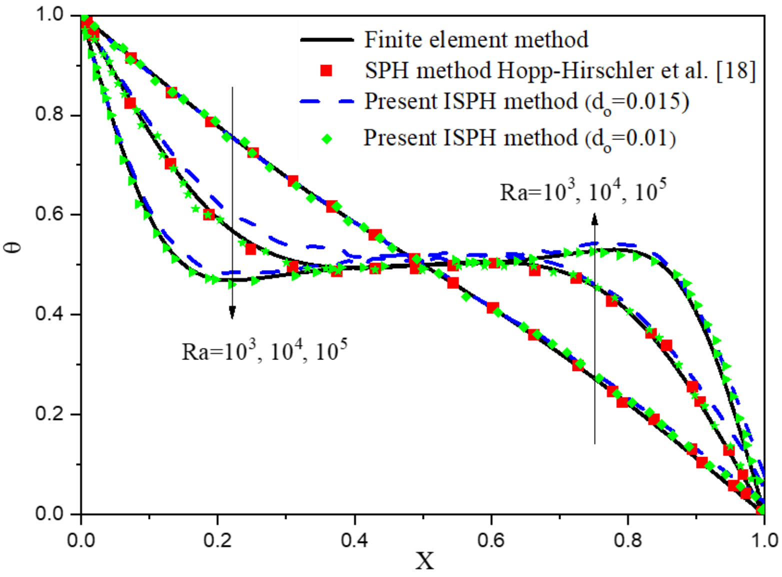

Figure 4. Comparison of temperature profiles (θ) along the $X-$axis between FEM results, the present ISPH method at two particle resolutions ($d_0 = 0.015$ and $d_0 = 0.01$), and SPH results from Hopp-Hirschler et al. [18].

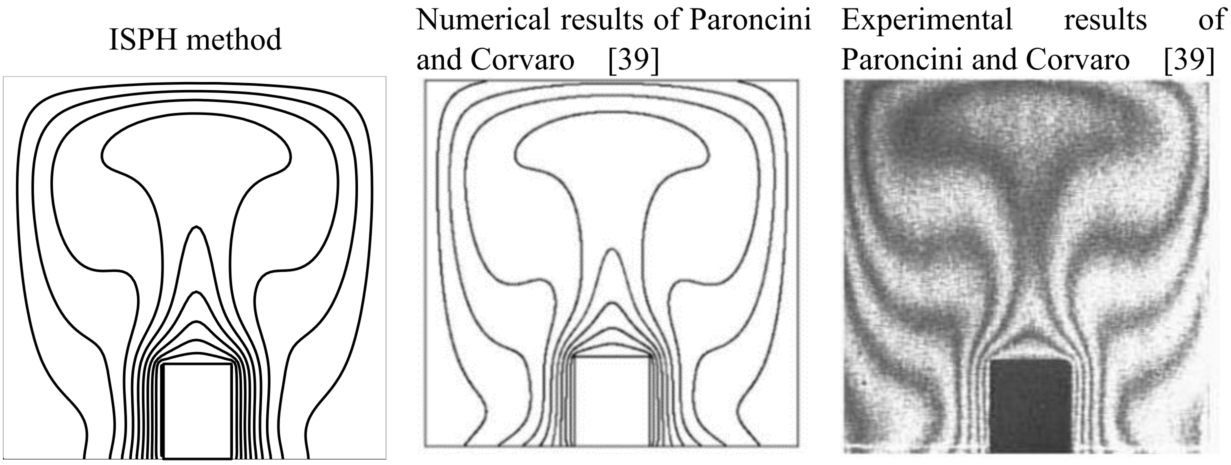
ISPH method
Numerical results of Paroncini and Corvaro [39]
Experimental results of Paroncini and Corvaro [39]

(a) $Ra = 1.02 \times 10^5$ and $\zeta = 0.25$

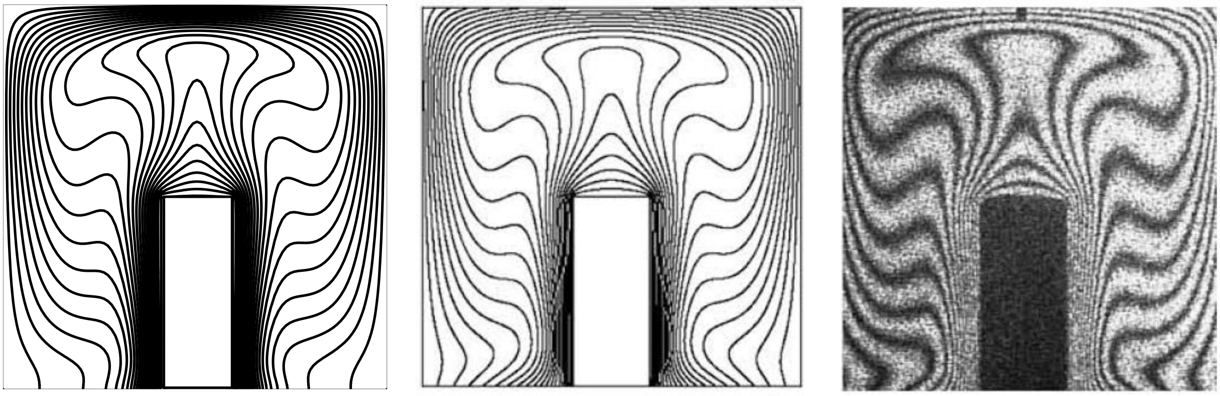

(b) $Ra = 2.25 \times 10^5$ and $\zeta = 0.5$

Figure 5. Comparison of isotherm lines between ISPH method, numerical/experimental results from Paroncini and Corvaro [39].

5. ANN modeling

The primary goal of employing the ANN model is to increase the accuracy of forecasting the thermosolutal convection of non-Newtonian NEPCM within a curvilinear cavity. The proposed ANN model is a great tool for dealing with the system's complexity, giving a robust and efficient method of forecasting the values of $\overline{Nu}$ and $\overline{Sh}$. In this study, the ANN model supplements the ISPH simulation by providing a more computationally efficient solution. This decrease in processing costs is especially useful for simulations with complicated geometries and huge dataset sizes. The ANN model is a form of machine learning model founded on connectionism's neuronal architecture principles that were discovered in animal brains' biological neural networks [40,41]. ANN is taught by experience rather than programming. ANN helps with data-related problems by constructing complicated nonlinear connections between the response variable and its predictors. The ANN model is utilized to predict the values of $\overline{Nu}$ and $\overline{Sh}$. The Levenberg-Marquardt algorithm (LMA) is a well-known trust region method for determining the minimum of a function across a range of parameters. A quadratic function defines a target function's trustworthy zone internally. The ANN model was built using the LMA and multilayer perceptron (MLP) architectures. MLP networks are commonly used in ANN models because of their layered structure, which significantly boosts their learning capacity [42]. Figure 6 portrays the network design and essential structure of the proposed MLP network architecture. The MLP network model's input layer defined the Soret and Dufour numbers (Sr & Du) and dimensionless time τ, while the output layer evaluated $\overline{Nu}$ and $\overline{Sh}$.

The MLP network model's hidden layer has fourteen neurons and consumes 4188 data points. Here, 15% is designated for testing, 15% for validation, and 70% for model training. The following are the transfer functions for the MLP network's output and hidden layers, mean squared error (MSE), coefficient of determination (R), and margin of deviation (MoD):

$$f(x) = tansig(x) = -1 + \frac{2}{e^{(-2x)} + 1}, \tag{46}$$

$$purelin(x) = x \tag{47}$$

$$MSE = \frac{1}{N}\sum_{i=1}^{N}(X_{targ\,(i)} - X_{pred(i)})^2, \tag{48}$$

$$R = \sqrt{1 - \frac{\sum_{i=1}^{N}\left(X_{targ(i)} - X_{pred(i)}\right)^2}{\sum_{i=1}^{N}\left(X_{targ(i)}\right)^2}}, \tag{49}$$

$$MoD = \left[\frac{X_{targ} - X_{pred}}{X_{targ}}\right]. \tag{50}$$

Figures 7–9 show the MSE, error histogram, and regression curves for MLP model training performance. Figure 7 depicts how MSE values fell with each epoch following the start of the training period. When each of the three data sets provided the best validation value, the MLP model's training phase was completed. Figure 8 depicts the error histogram for the MLP model during training, which indicates that the error values are primarily grouped around the zero-error line. The numerical values of the errors were small. Figure 9 shows the regression curve for the MLP model, indicating that $R = 1$ is utilized for training, validation, and testing. Figure 10 illustrates the MLP model's gradient state. The graphical results show that the proposed MLP model converges at epoch 7, with a gradient value of $4.574e^{-06}$ and Mu value of $1e^{-08}$.

Principal component analysis (PCA) transforms the input data (X) into new axes defined by the eigenvectors (v_i) of the covariance matrix. The transformation is:

$$PC_i = X \cdot v_i \quad \text{for } i = 1,2, \dots, k, \tag{51}$$

where PC_i is the i-th principal component, and v_i is its corresponding eigenvector. Figure 11 displays the $\overline{Nu}$ and $\overline{Sh}$ values obtained using the ANN model and the target values. The top row presents the original plots with data points indexed sequentially, highlighting the accurate match between the ANN predictions and the actual values for both $\overline{Nu}$ and $\overline{Sh}$. The bottom row provides PCA-based plots, where the X −axis reflects the primary component of the input data, derived using Principal Component Analysis (PCA). These plots offer a more meaningful representation of the variance in the input parameters, emphasizing the ANN model's ability to predict $\overline{Nu}$ and $\overline{Sh}$ values with precision. The perfect alignment of the actual and predicted values in both representations confirms the model's accuracy.

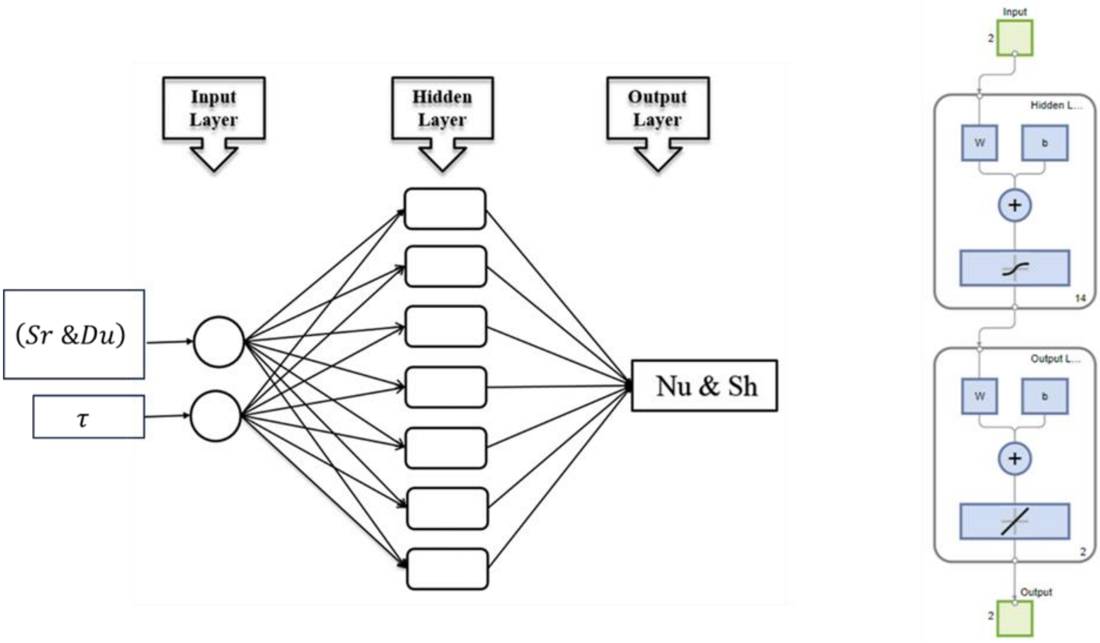

Figure 6. The network design and essential structure of the proposed MLP network architecture.

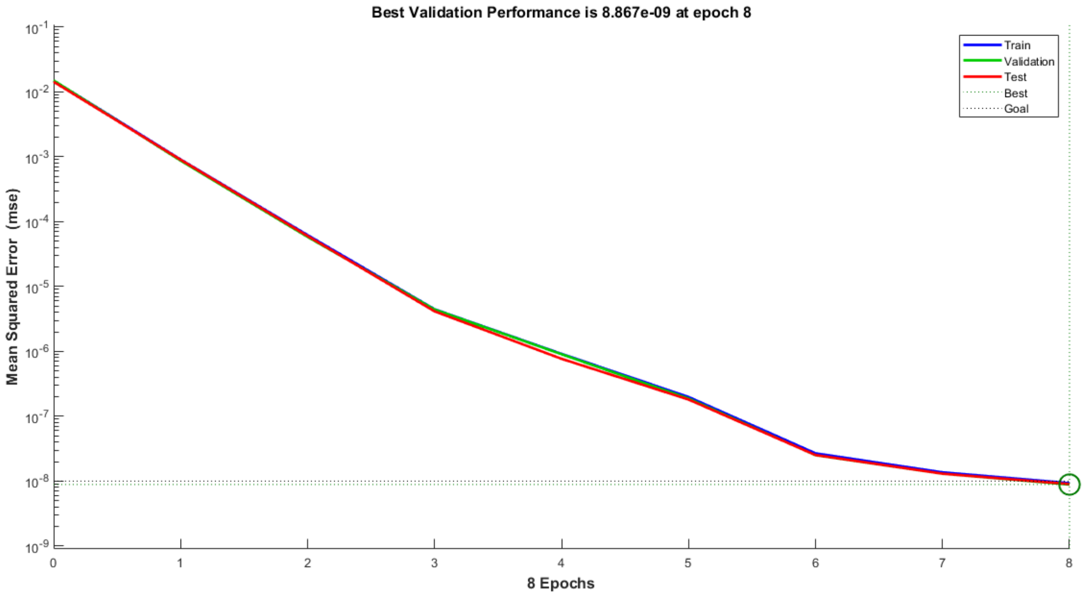

Figure 7. Training, validation, and test mean squared error (MSE) over 8 epochs, showing the best validation performance achieved at epoch 8.

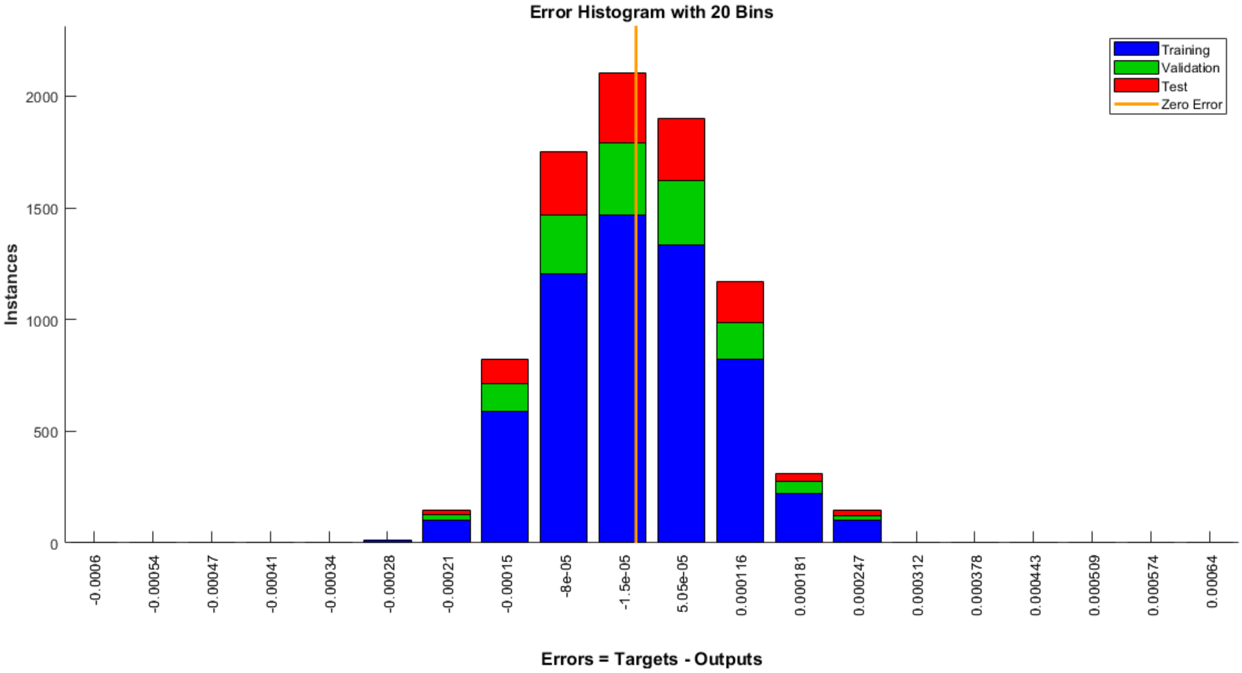

Figure 8. Error histogram with 20 bins showing the distribution of errors for training, validation, and test data.

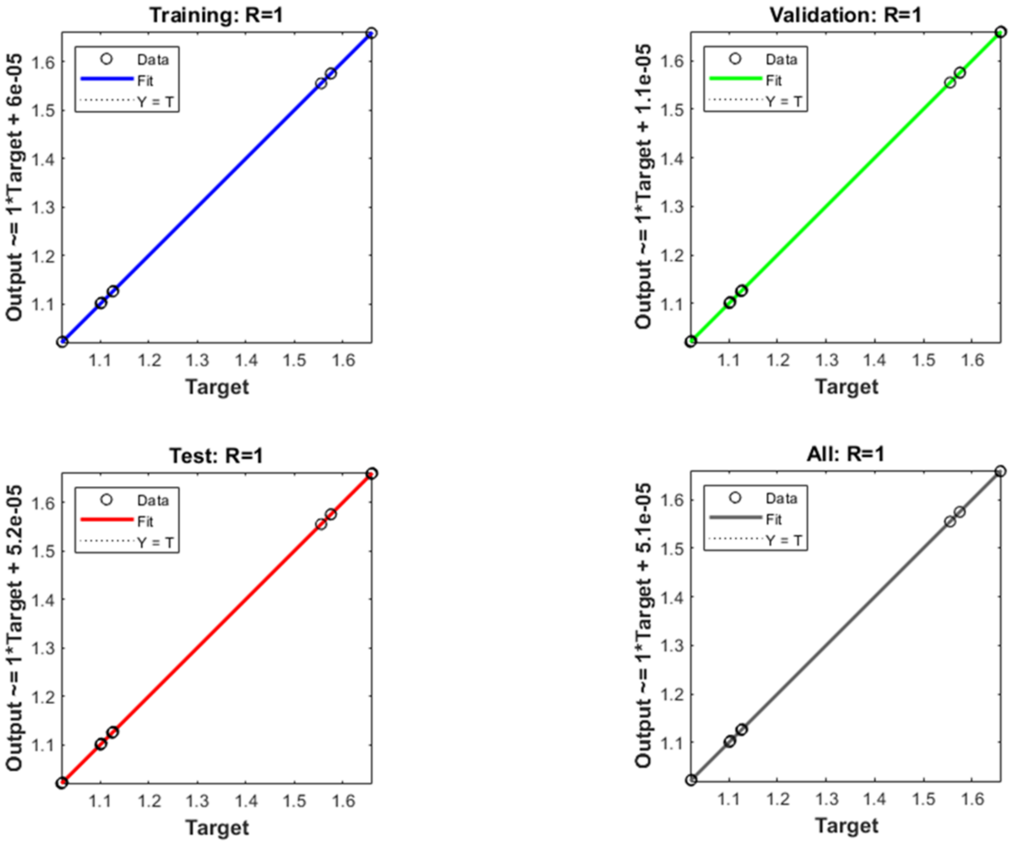

Figure 9. Regression plots showing the relationship between targets and outputs for training, validation, test, and combined datasets with correlation coefficients (R) close to 1, indicating high predictive accuracy**.**

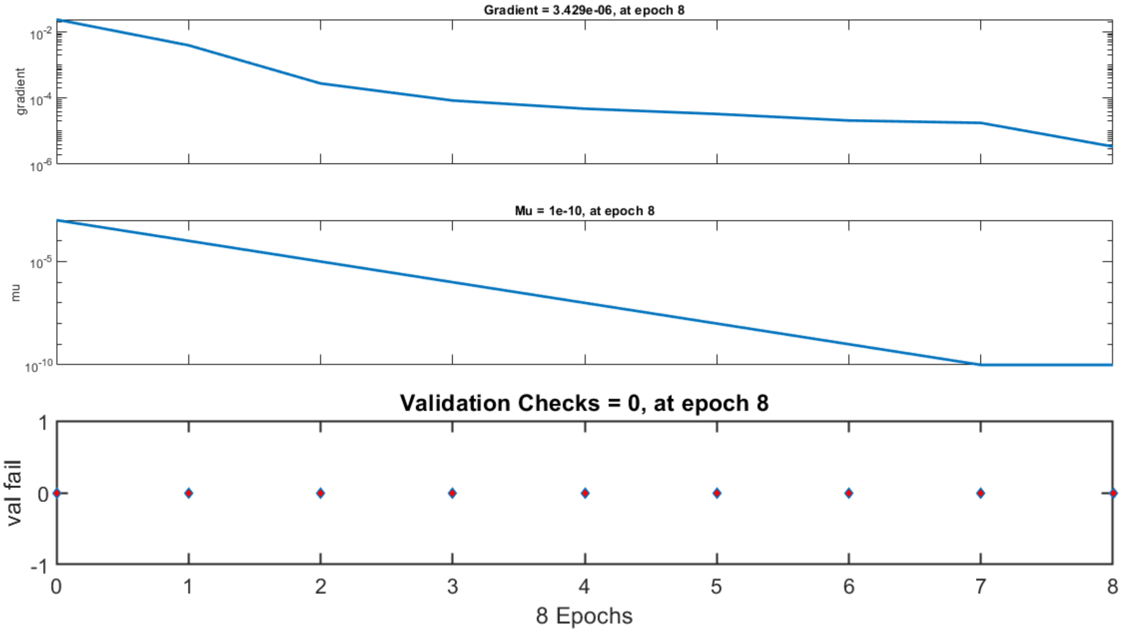

Figure 10. Training progress plots showing gradient reduction, mu updates, and validation checks across 8 epochs.

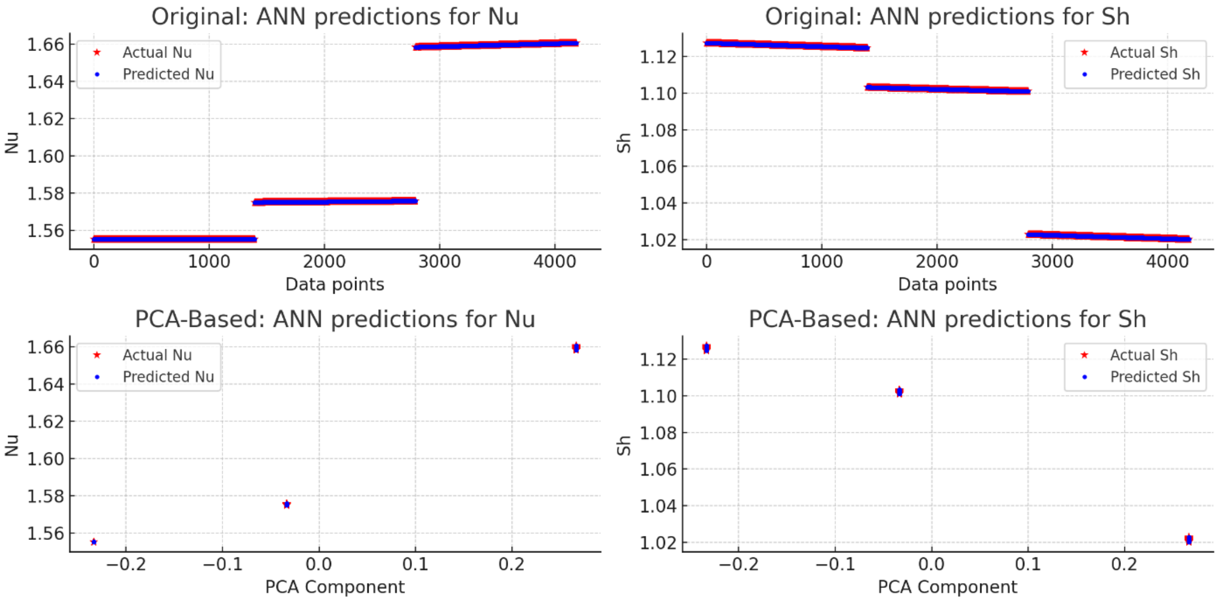

Figure 11. ANN predictions versus actual values for the average Nusselt $\overline{Nu}$ and Sherwood $\overline{Sh}$ numbers across data points.

6. Results and discussion

In this section, we provide the ISPH numerical simulations for pertinent parameters like Frank-Kamenetskii number $Fk = 0 - 1$, Cattaneo-Christov (Ca-Ch) heat, mass transfer parameters $\delta_\theta = \delta_\Phi = 0 - 0.2$, Hartmann number $Ha = 0 - 60$, buoyancy ratio parameter $N = -2 - 4$, power law index parameter $n = 1.1 - 1.4$, Rayleigh number $Ra = 10^3 - 10^5$, Soret – Dufour numbers $Sr = Du = 0 - 0.5$, and fusion temperature $\theta_f = 0.1 - 0.9$. Here, C1 symbolizes high temperature and concentration at the top and bottom of the curved lines, and low temperature and concentration in the vertical walls and inner ellipse. C2 depicts high temperature and concentration on the boundary walls, while low temperature and concentration are depicted on an inner ellipse. Figure 12 indicates the impacts of Frank-Kamenetskii number Fk on isotherms θ, heat capacity ratio Cr, isoconcentration Φ, and velocity field V. The isotherms are strengthened across a curvilinear cavity under an increment in Fk, demonstrating enhanced thermal gradients due to intensified heat release from exothermic reactions. This behavior underscores the significance of Fk as a parameter in controlling heat generation within reactive systems, influencing the temperature distribution across the medium. Consequently, the Cr contour adjusts in response to variations in Fk, reflecting changes in the balance between heat storage and transfer. The isoconcentration Φ shows a minor response to Fk variations, indicating that the chemical concentration profile remains relatively stable despite increased thermal effects. The velocity field experiences fluctuations at $C1$, while at $C2$, an increase of 2.31% is observed, highlighting the role of Fk in enhancing convective flow and influencing the overall fluid movement within the cavity. These findings illustrate the critical impact of Fk on thermal management and flow behavior in systems involving exothermic reactions. Figure 13 illustrates the impacts of the Cattaneo heat (δ_θ) and mass (δ_Φ) transmission parameters on the isotherms (θ), heat capacity ratio (Cr), concentration (Φ), and velocity field (V). An increment in δ_θ and δ_Φ results in a noticeable decrease in the strength of isotherms at both C1 and C2. This reduction reflects the influence of non-Fourier heat and mass transfer effects, which slow the propagation of thermal and concentration waves, leading to less steep temperature gradients. The decreased strength of θ around the inner ellipse highlights areas of lower temperature and concentration, impacting thermal and solutal stability within the cavity. As a response to the increased δ_θ and δ_Φ, the Cr contour shows upward and downward shifts, indicating that the thermal storage properties adapt to altered temperature distributions, which are influenced by delayed heat conduction. This effect emphasizes the importance of these parameters in defining the system's response to rapid thermal and solutal variations, especially in environments where wave-like transport phenomena are present. The concentration (Φ) also weakens across the curvilinear cavity at C1 and C2, further confirming the slower mass diffusion attributed to the higher δ_θ and δ_Φ. The velocity field undergoes a significant decrease, showing reductions of 44.1% and 48.9% at C1 and C2, respectively, when δ_θ and δ_Φ increase from 0 to 0.2. This reduction illustrates the strong coupling between thermal and solutal wave transport and convective motion, underscoring the importance of δ_θ and δ_Φ in managing heat and mass transfer rates within such systems, which is crucial for optimizing processes involving rapid changes in temperature and concentration. Figure 14 illustrates the influence of the Hartmann number (Ha) on the isotherms (θ), heat capacity ratio (Cr), concentration (Φ), and velocity field (V). The Hartmann number represents the ratio of electromagnetic forces to viscous forces in a conducting fluid, originally defined by Julius Hartmann (1881−1951). At higher Ha values, the presence of the Lorenz force significantly impacts the flow by slowing the velocity field and suppressing convection. This braking effect, induced by the magnetic field, results in a dramatic decrease in the convective strength, reducing the overall motion within the cavity. This magnetic damping is a crucial aspect in controlling heat transfer rates and stabilizing fluid behavior in applications where magnetic fields are employed to modulate fluid dynamics. The reduction in the velocity field, defined by its peak values, underscores the capacity of Ha to act as a regulatory factor for convective flow. This is particularly important for applications in magnetohydrodynamics (MHD) where magnetic fields are used to manage flow stability and thermal characteristics in various systems. The Cr contour shows only slight variations in response to changes in Ha, indicating that the heat capacity properties remain relatively stable despite significant electromagnetic intervention. This stability implies that, while the velocity field is suppressed, the inherent thermal storage properties of the fluid are not greatly affected, enabling controlled thermal energy distribution even under magnetic influence. The isotherms (θ) exhibit moderated gradients as Ha increases, illustrating the reduced convective transport and highlighting how the magnetic field dampens the temperature distribution within the cavity. Similarly, the concentration field (Φ) is impacted to a lesser extent, maintaining its structure while experiencing a subdued transport rate due to the weakened convective currents. These findings emphasize the role of (Ha) in modulating both thermal and flow characteristics, which is essential for optimizing heat and mass transfer processes in MHD applications where magnetic field manipulation is used for improved process control and stability. Figure 15 shows the impacts of buoyancy ratio parameter N on θ, Cr, Φ, and V. The buoyancy ratio, which is a measure of fluid density contributions by the two solutes and shows the degree of system disequilibrium, has steadily shifted from near stable to highly unstable. Increasing N enhances slightly the isotherms, Cr, and isoconcentration at C1 and C2. The velocity field is strongly enhanced according to an increment in N. At $N = -2$, the maximum of V appears at the top area over an ellipse while it appears at the lower area below an ellipse at $N \geq 0$. Figure 16 represents the influences of power-law index n on θ, Cr, Φ, and V. The Power Law model categorizes fluids as Newtonian $(n = 1)$, Shear Thinning (pseudoplastic) $(0 < n < 1)$, and Shear Thickening (dilatant) $(n > 1)$. As n is increased from 1.1 to 1.4, there is a noticeable yet slight enhancement in the temperature distribution θ and concentration Φ at C1 and C2. This enhancement suggests that the flow characteristics change to accommodate more resistance to deformation as the fluid transitions towards a more shear-thickening behavior. The heat capacity ratio Cr contour displays slight shifts with changes in n at C1 and C2. These minor changes indicate that the capacity of the fluid to store thermal energy is somewhat affected by the power-law index but not drastically, reflecting a stable thermal response even as the fluid's rheological properties shift. A significant impact is observed in the velocity field, which decreases markedly by 64.68% at C1 and 64.66% at C2 when n is increased from 1.1 to 1.4. This reduction in velocity is attributed to the increased resistance to flow present in shear-thickening fluids, where the effective viscosity increases with the rate of shear strain. These characteristics highlight the importance of the power-law index in controlling the convective behavior of non-Newtonian fluids. The sharp decline in the velocity field points to a dampened convective motion, leading to reduced momentum transfer within the fluid. These findings underscore the significance of the power-law index in determining the overall thermal and flow dynamics in non-Newtonian fluid systems. Adjusting n can be a strategic means of controlling heat and mass transfer in engineering applications where precise modulation of fluid behavior is required, such as in industrial processes involving complex fluids or in systems where customized thermal management is essential. Figure 17 indicates the impacts of Ra on θ, Cr, Φ, and V. Ra is an indicator that describes heat transport in natural convection processes. Convection does not occur below the critical Ra; instead, heat is transmitted by thermal conduction. Above a certain Ra, heat is transported via convection. The distributions of θ and Φ are enhanced according to an increase in Ra. The velocity field is strongly raised according to an increase in Ra at C1 and C2. Figure 18 presents the effects of the Soret number (Sr) and the Dufour number (Du) on θ, Cr, Φ, and V. The Soret number (Sr) quantifies the ratio of temperature gradients to concentration gradients, highlighting the influence of thermal diffusion on mass transport. Moreover, the Dufour number (Du) represents the contribution of concentration gradients to thermal energy flux within the flow, capturing the cross-coupling between heat and mass transfer mechanisms. An increase in (Sr) and (Du) leads to an enhancement in the distribution of the concentration field Φ, indicating stronger solutal transport effects and emphasizing the interplay between thermal and concentration gradients in driving diffusion processes. This enhancement showcases how these coupled phenomena facilitate the redistribution of solutes within the flow, which can be pivotal in applications involving mixed convection and thermosolutal interactions. The distribution of the temperature θ and the heat capacity ratio (Cr) at C1 and C2 are only slightly influenced by the increase in Sr and Du. This indicates that while mass transfer effects are more pronounced with higher Sr and Du, the overall temperature field and thermal storage properties maintain relative stability. Such behavior highlights that the energy transfer in the system is not drastically affected by the solutal cross-diffusion effects. A more significant impact is observed in the velocity field, which experiences an increase of 34.17% at C1 and 29.73% at C2 as Sr and Du rise from 0 to 0.5. This boost in the velocity field suggests enhanced convective currents driven by the combined thermal and concentration gradients. The increased flow velocity underscores the role of the Soret and Dufour effects in augmenting fluid motion through the synergistic influence of heat and mass fluxes. These findings emphasize the importance of Sr and Du as key parameters in systems involving double diffusion, where the interplay between temperature and concentration gradients plays a critical role. Understanding their impacts can aid in optimizing processes involving heat and mass transfer, such as in chemical reactors, enhanced oil recovery, and various environmental engineering applications where precise control over diffusion and convection is required. Figure 19 shows the impacts of θ_f on a heat capacity ratio (Cr). Increasing θ_f causes the Cr contour to move towards the top/bottom of a curvilinear at $C1$ and extend towards the curvilinear sides at $C2$. The intensity of the Cr contour diminishes as Cr increases. It is generally known that θ_f is important in altering the placements and strength of Cr contour within a curvilinear cavity. Figure 20 presents the average $\overline{Nu}$ and $\overline{Sh}$ under the variations of N, Ha, $(Sr\&\,Du)$, and $(\delta_\theta\ \&\ \delta_\Phi)$ at C1 and C2. The average Nusselt number $\overline{Nu}$, representing the rate of convective heat transfer, is consistently higher under boundary case C1 compared to C2, indicating more effective heat transfer when C1 conditions are applied. This behavior underscores the importance of boundary definitions in determining heat transfer performance. An increase in N, Ha, and $Sr\&\,Du$ enhances $\overline{Nu}$, demonstrating that non-Newtonian properties, electromagnetic effects, and coupled thermal-solutal interactions significantly boost heat transfer efficiency. The $\delta_\theta\ \&\ \delta_\Phi$ parameters show minor effects on $\overline{Nu}$, suggesting that wave-like transport phenomena impact transient responses more than steady-state behavior. The average Sherwood number $(\overline{Sh})$, which measures convective mass transfer, increases under all parameters examined, including N, Ha, and $Sr\&\,Du$ and $\delta_\theta\ \&\ \delta_\Phi$. Initially, the C1 case supports higher $\overline{Sh}$ than C2, indicating that the initial mass transfer benefits more under C1 conditions. However, at steady-state, C2 exhibits a higher $\overline{Sh}$ compared to C1, implying that over time, C2 becomes more effective for mass transfer, likely due to a redistribution of concentration gradients influenced by boundary conditions. These findings demonstrate the critical role of boundary conditions in influencing heat and mass transfer within a curvilinear cavity. Understanding how boundary cases like C1 and C2 affect $\overline{Nu}$ and $\overline{Sh}$ is essential for designing and optimizing systems involving non-Newtonian fluids, MHD flows, and applications where thermal and mass transfer control is vital.

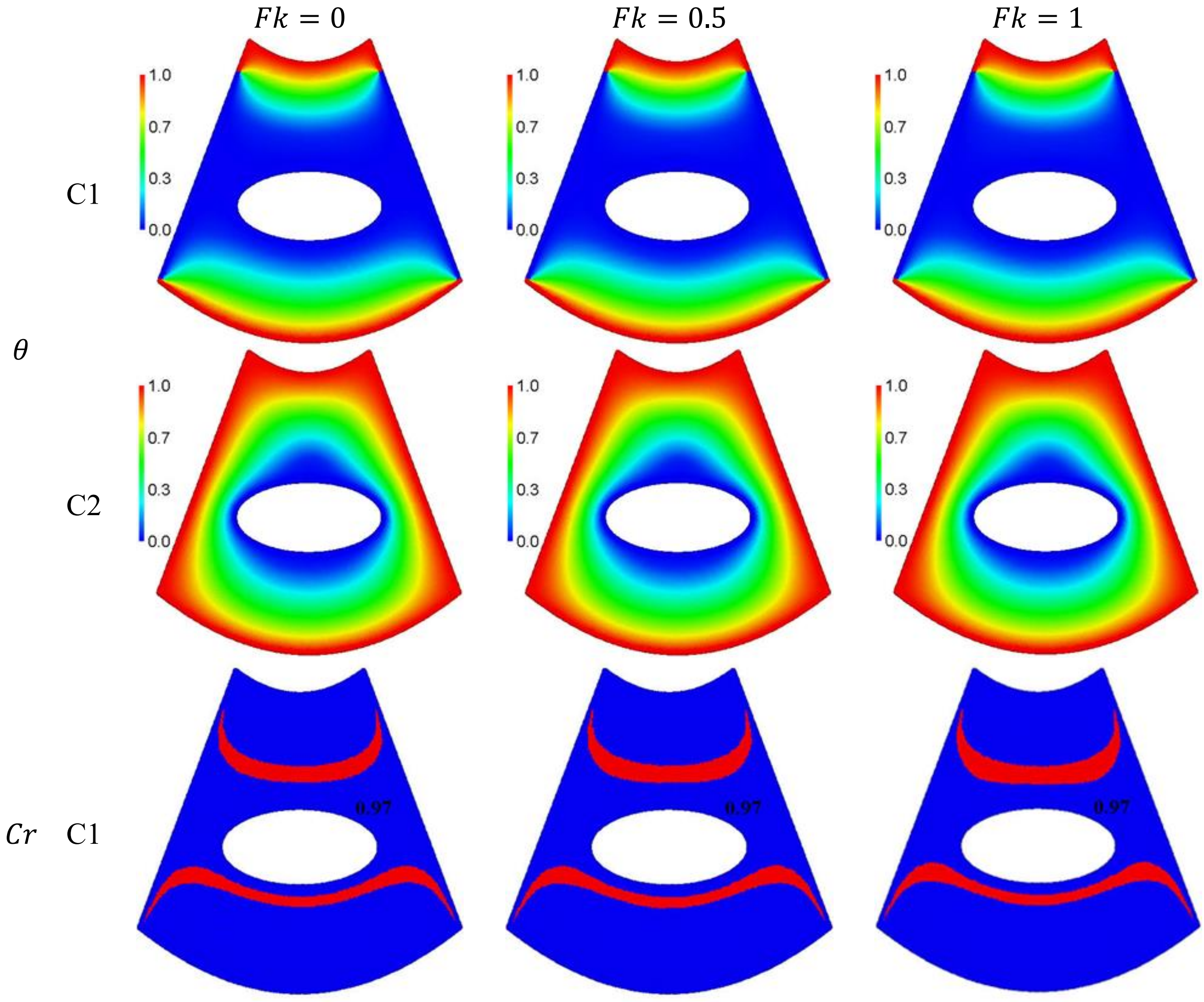

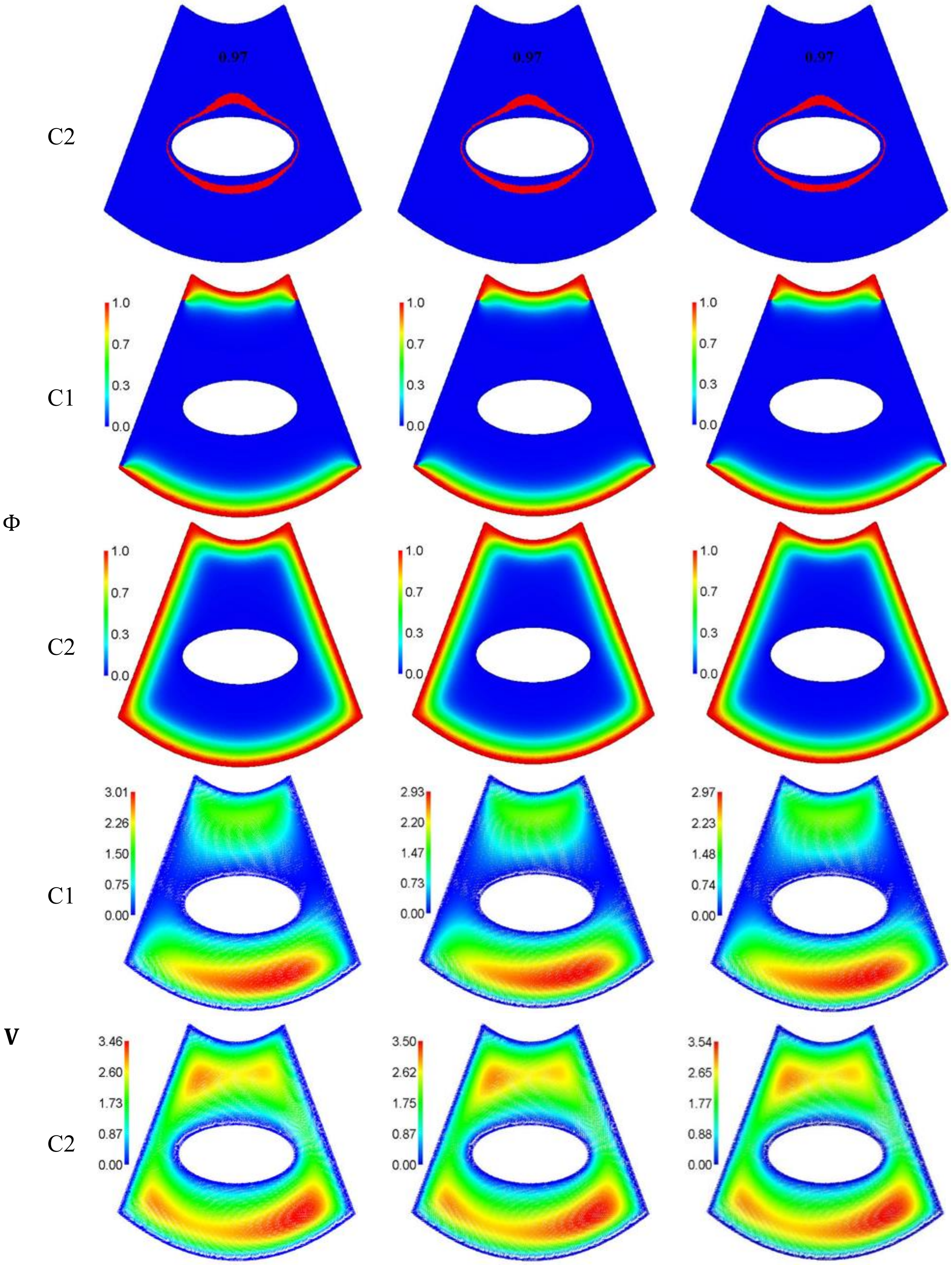

Figure 12. Impacts of Fk on θ, Cr, Φ, and $\mathbf{V}$.

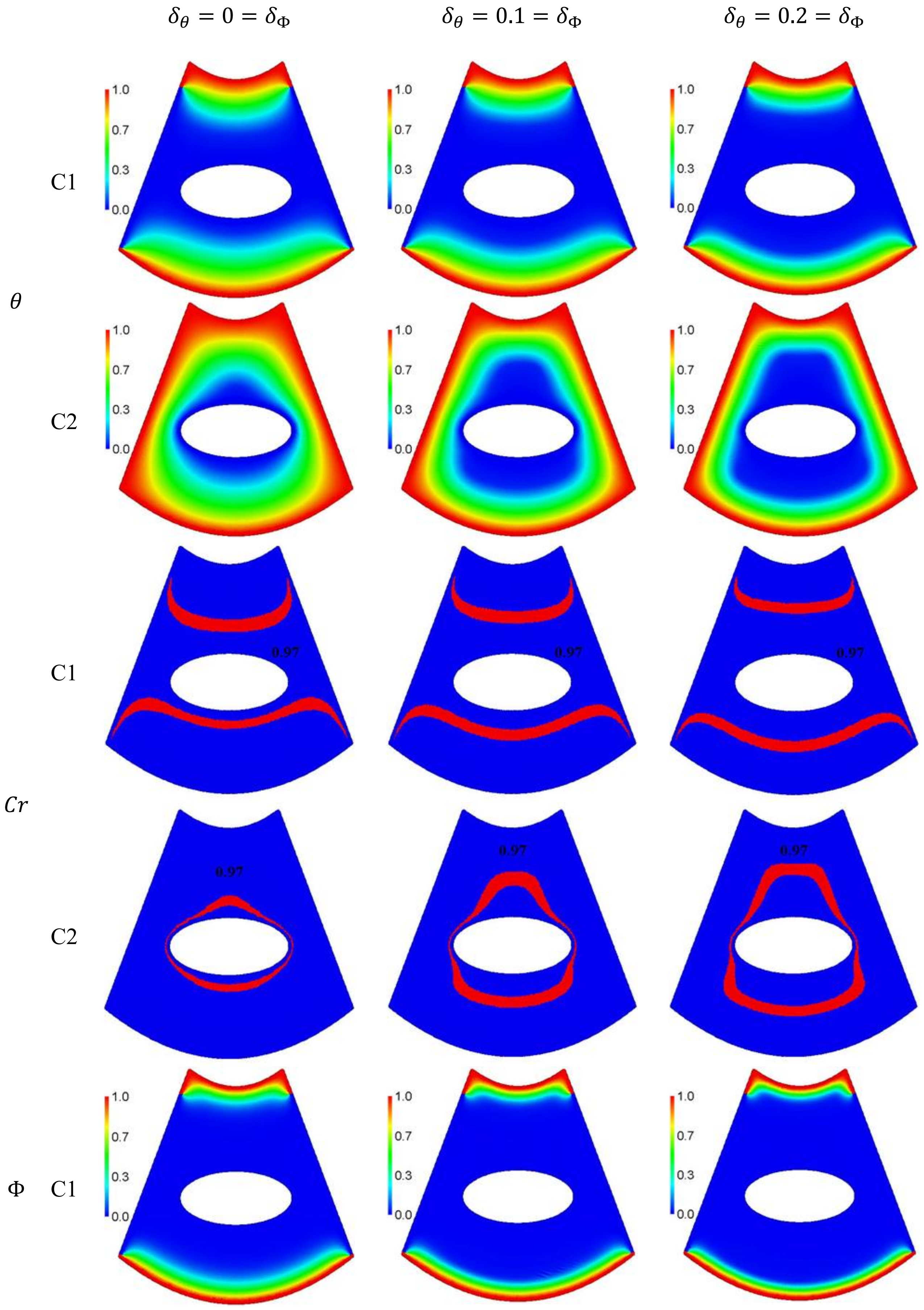
$\delta_\theta = 0 = \delta_\Phi$
$\delta_\theta = 0.1 = \delta_\Phi$
$\delta_\theta = 0.2 = \delta_\Phi$
θ
C1
C2
Cr
C1
C2
Φ
C1
1.0
0.7
0.3
0.0
0.97

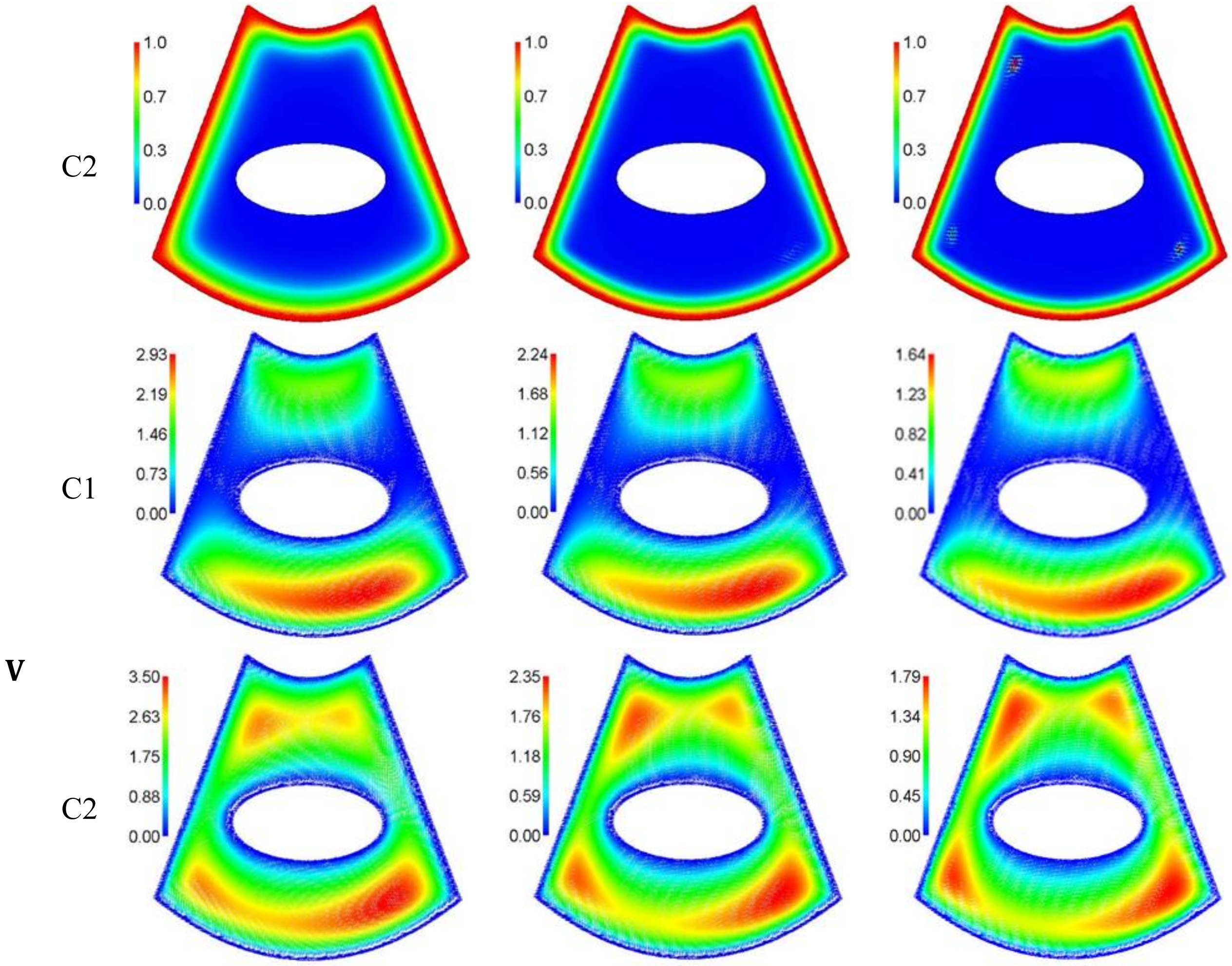

Figure 13. Impacts of $(\delta_\theta \,\&\, \delta_\Phi)$ on θ, Cr, Φ, and $\mathbf{V}$.

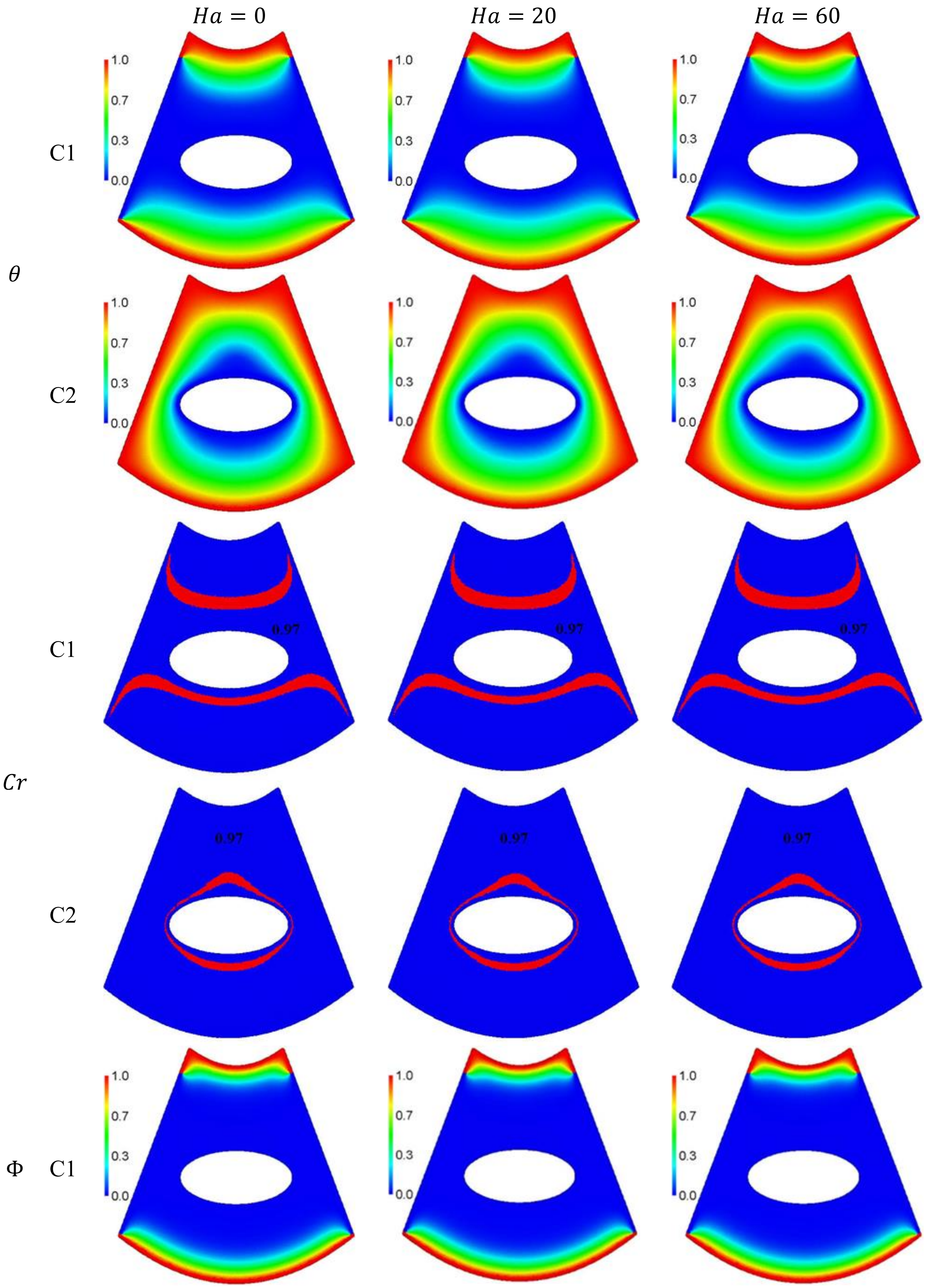
Ha = 0
Ha = 20
Ha = 60
θ
C1
C2
Cr
C1
C2
Φ
C1
1.0
0.7
0.3
0.0
0.97

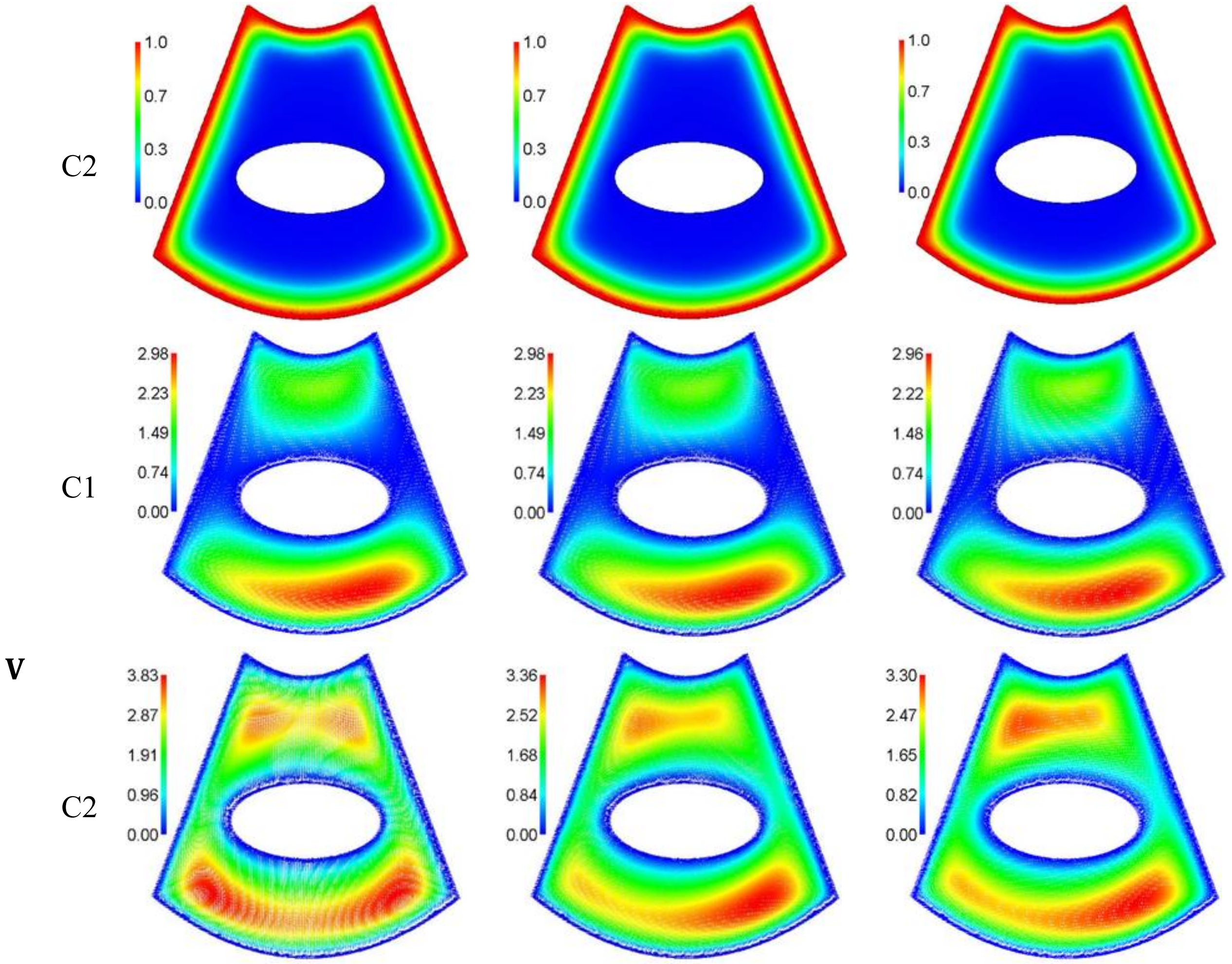

Figure 14. Impacts of Ha on θ, Cr, Φ, and $\mathbf{V}$.

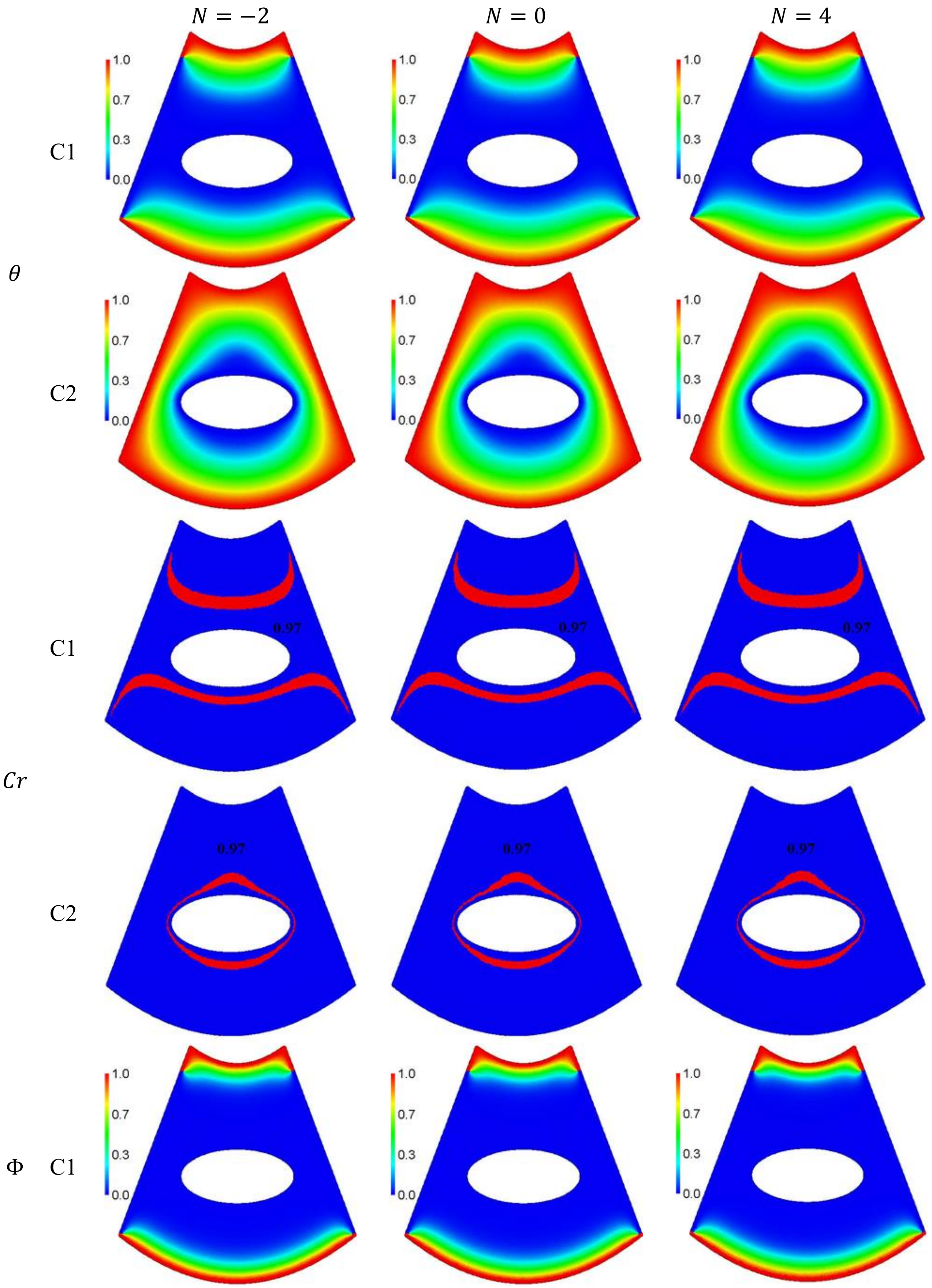
$N=-2$
$N=0$
$N=4$
θ
C1
C2
Cr
C1
C2
Φ
C1
1.0
0.7
0.3
0.0
0.97

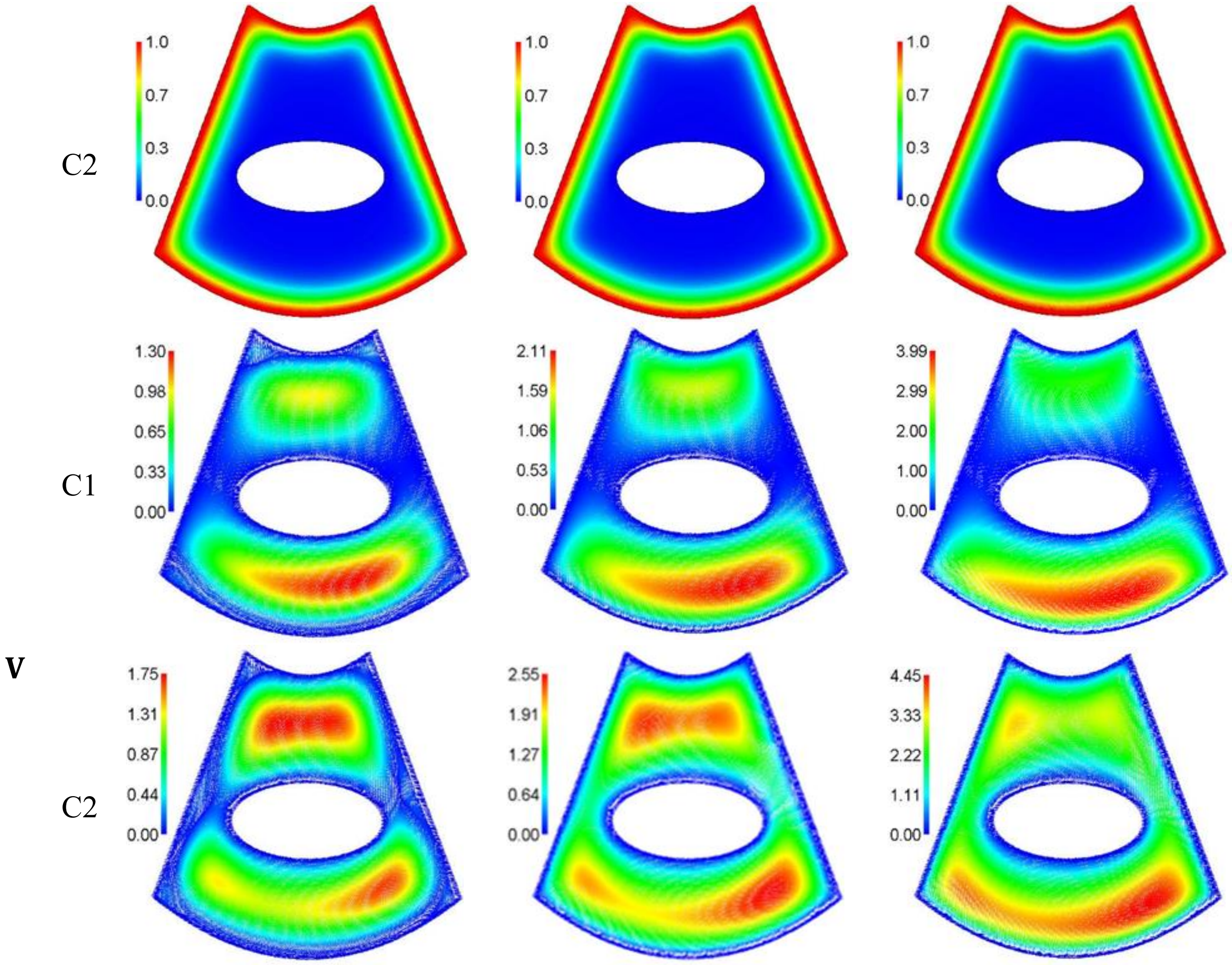

Figure 15. Impacts of N on θ, Cr, Φ, and $\mathbf{V}$.

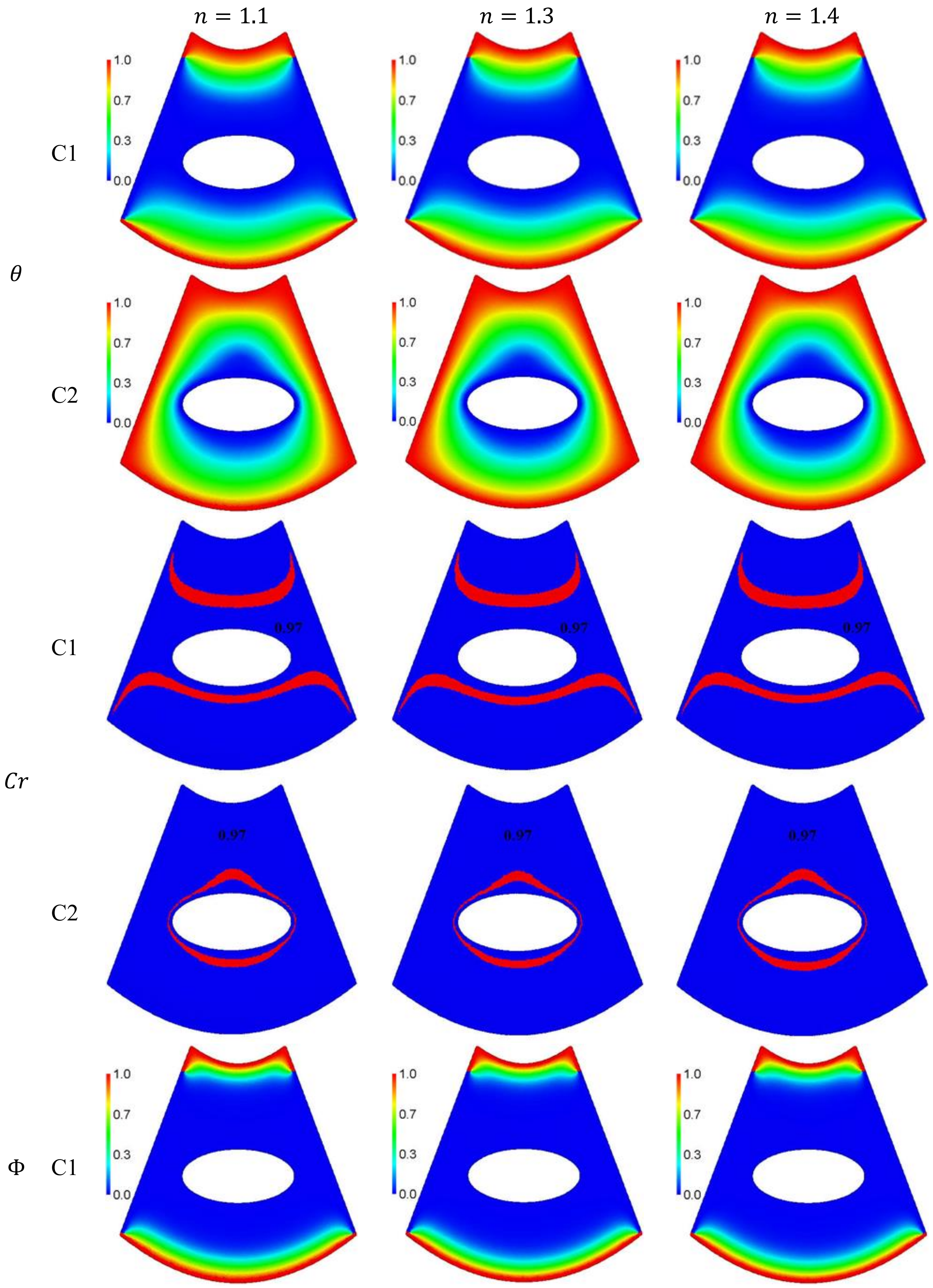
$n = 1.1$
$n = 1.3$
$n = 1.4$
θ
C1
C2
Cr
C1
C2
Φ
C1
1.0
0.7
0.3
0.0
0.97

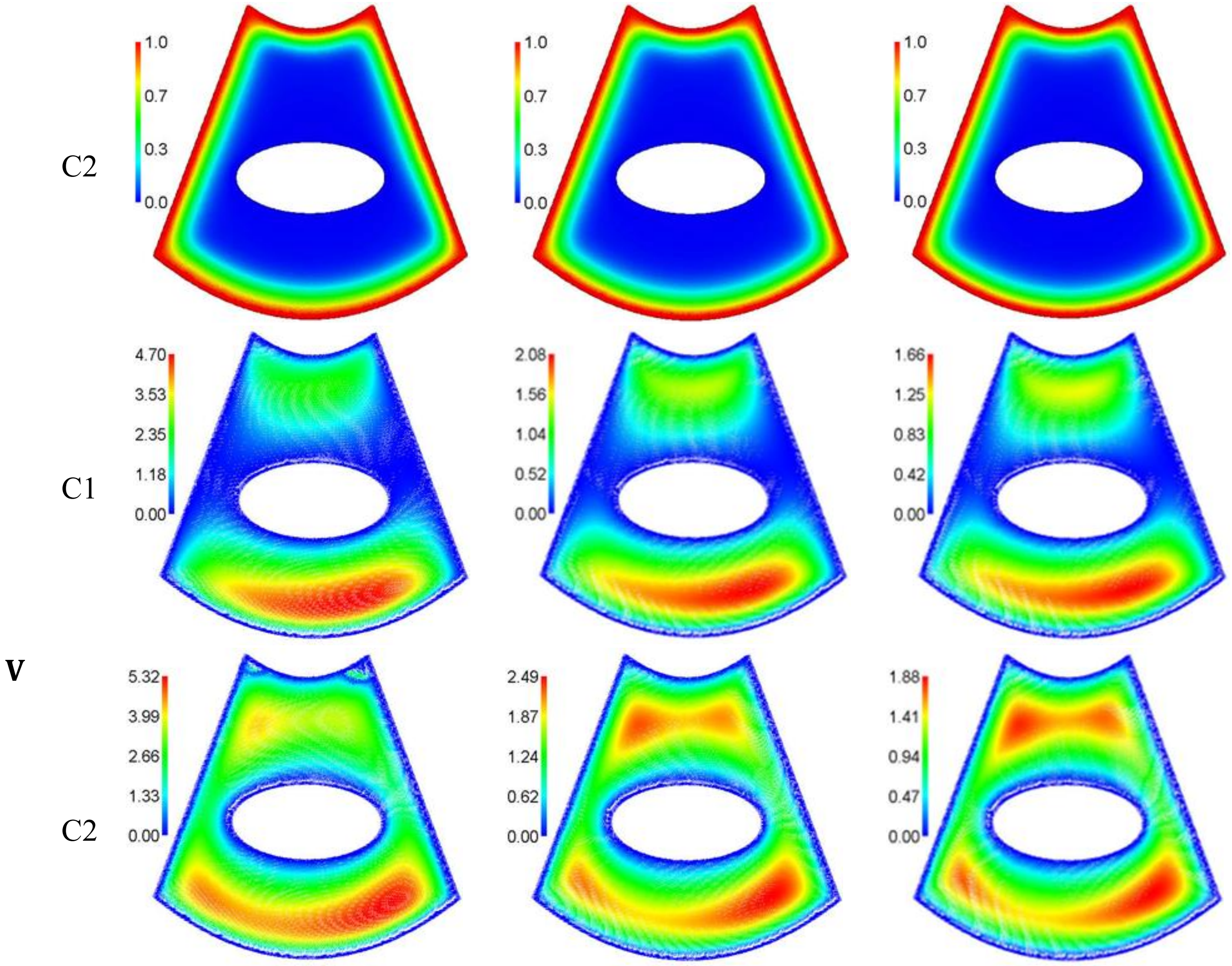

Figure 16. Impacts of n on θ, Cr, Φ, and $\mathbf{V}$.

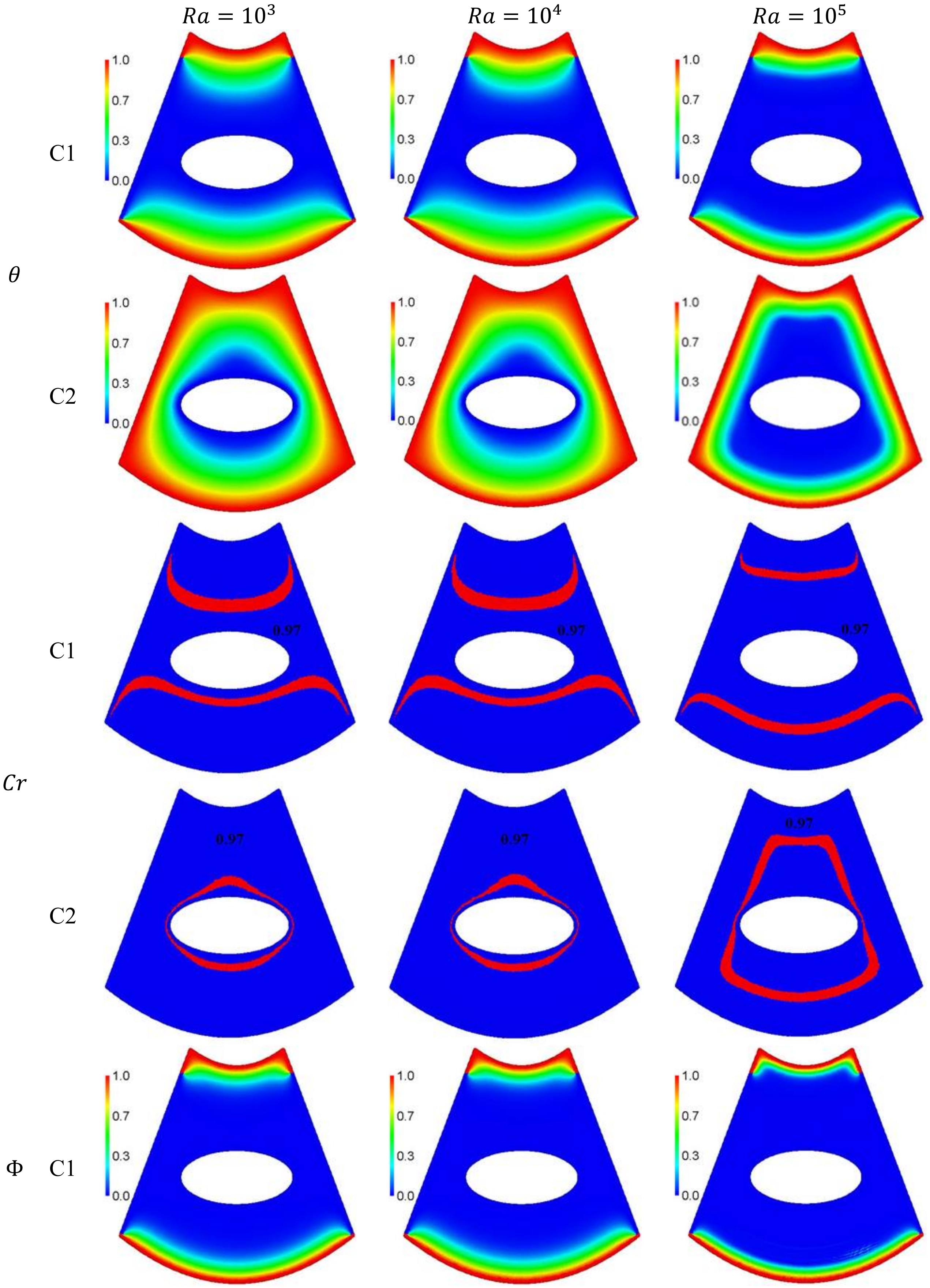
$Ra = 10^3$
$Ra = 10^4$
$Ra = 10^5$
θ
C1
C2
Cr
C1
C2
Φ
C1
1.0
0.7
0.3
0.0
0.97

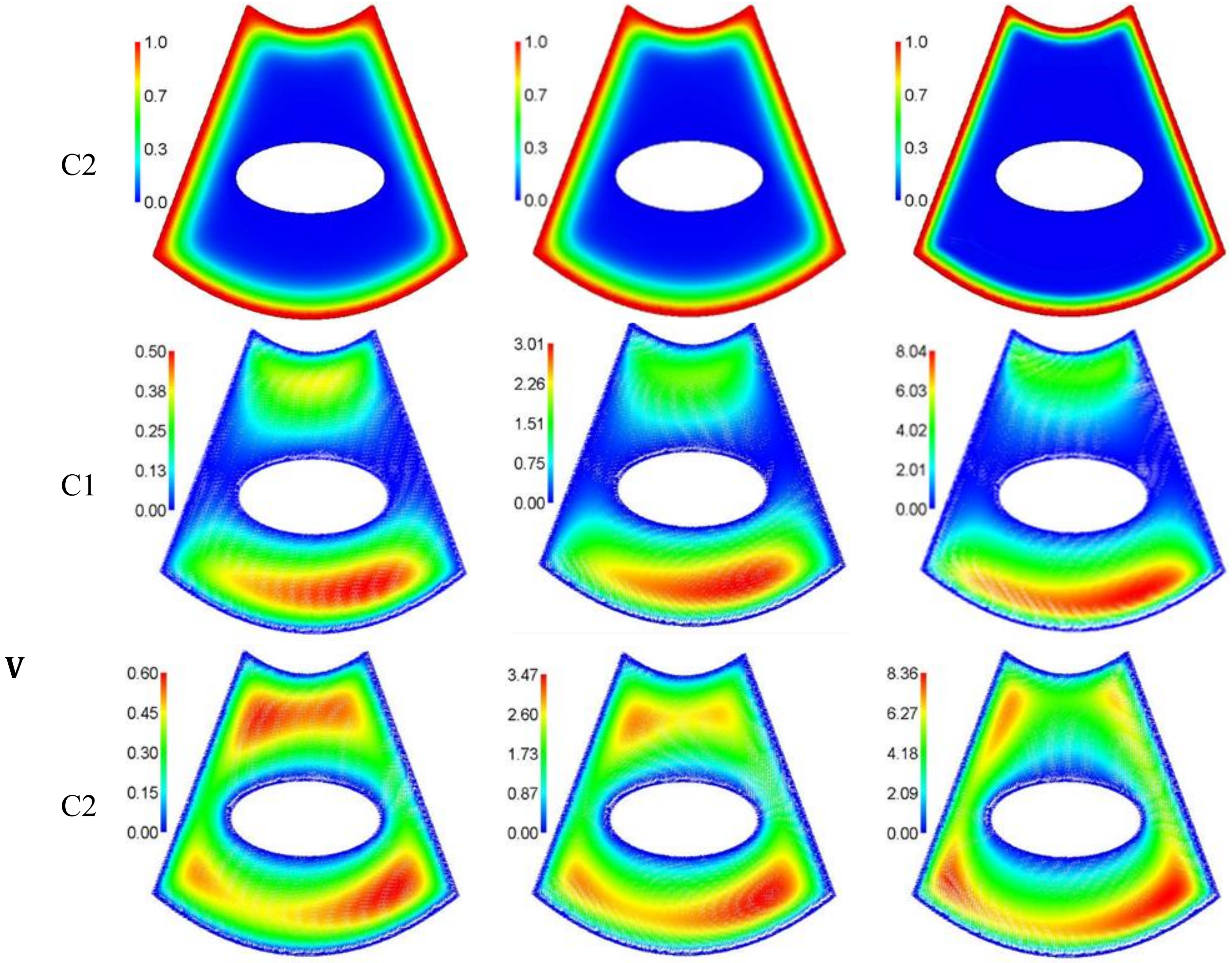

Figure 17. Impacts of Ra on θ, Cr, Φ, and $\mathbf{V}$.

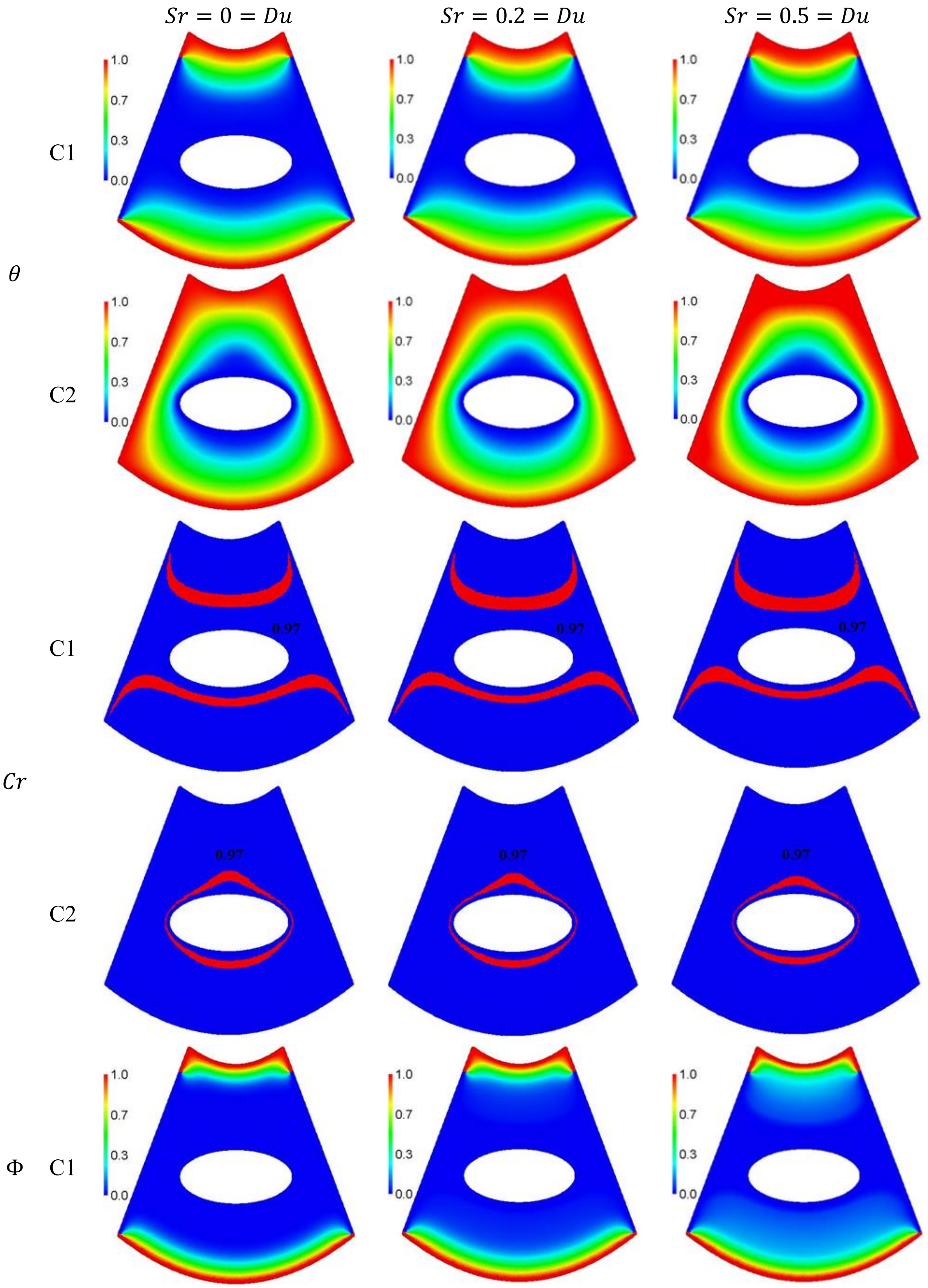
$Sr = 0 = Du$
$Sr = 0.2 = Du$
$Sr = 0.5 = Du$
θ
C1
C2
Cr
C1
C2
Φ
C1
1.0
0.7
0.3
0.0
0.97

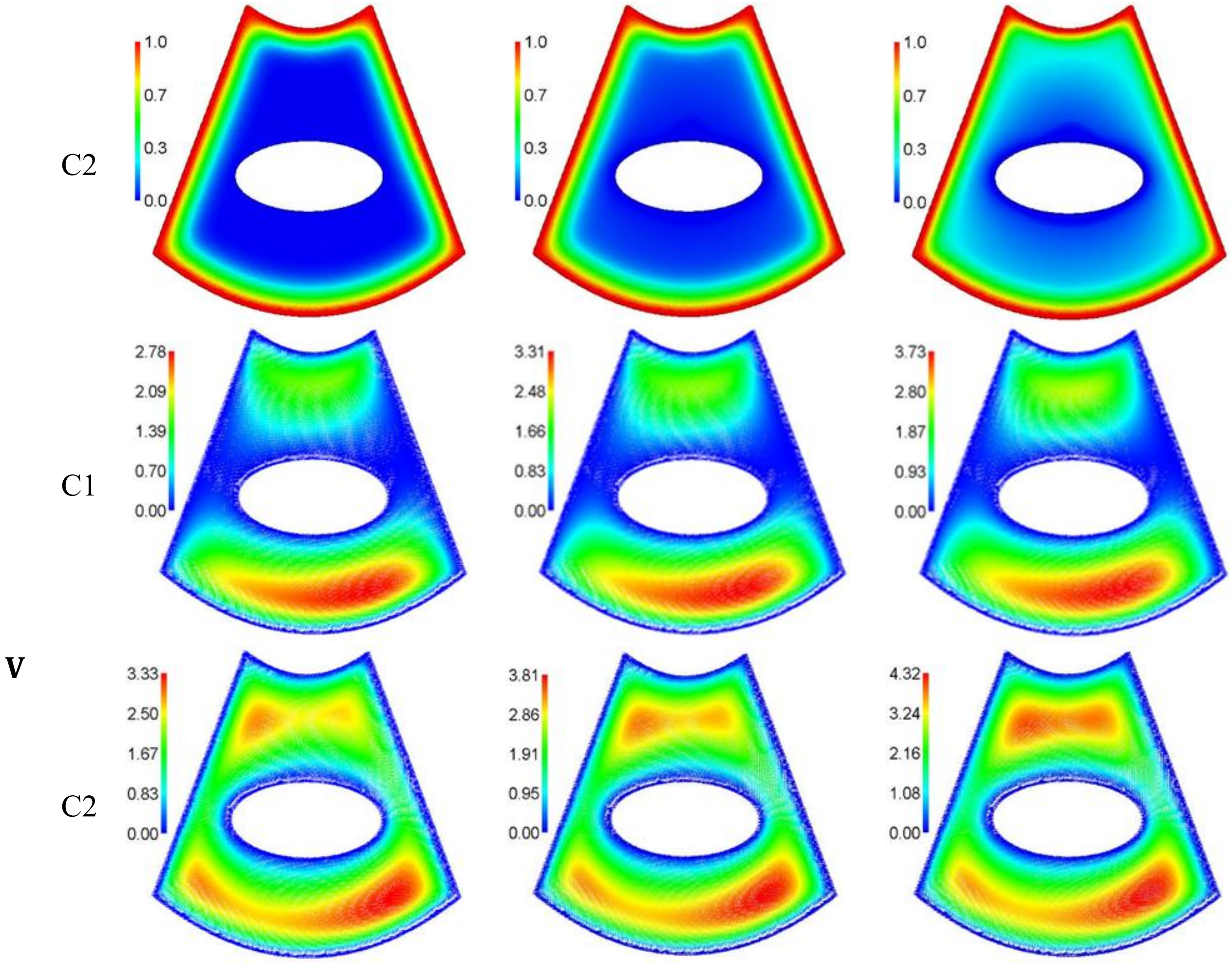

Figure 18. Impacts of $(Sr \,\&Du)$ on θ, Cr, Φ, and $\mathbf{V}$.

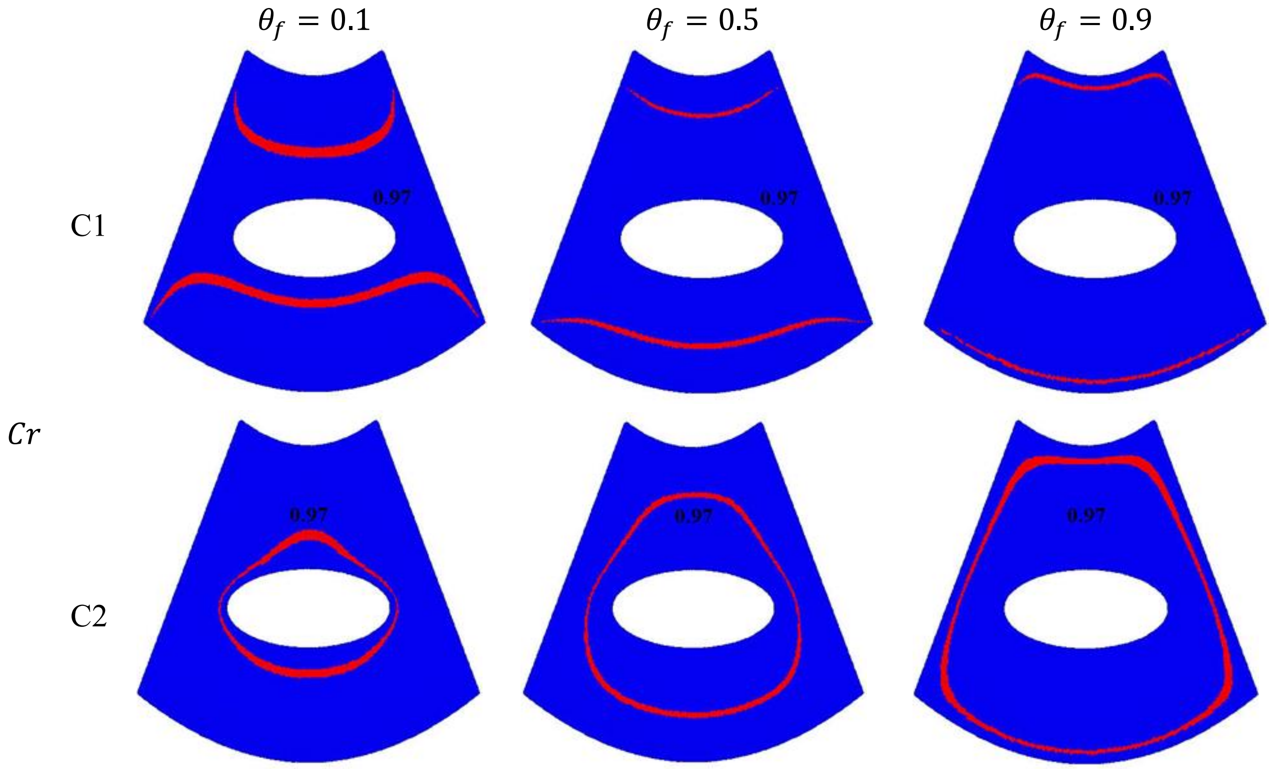

Figure 19. Impacts of θ_f on θ, Cr, Φ, and $\mathbf{V}$.

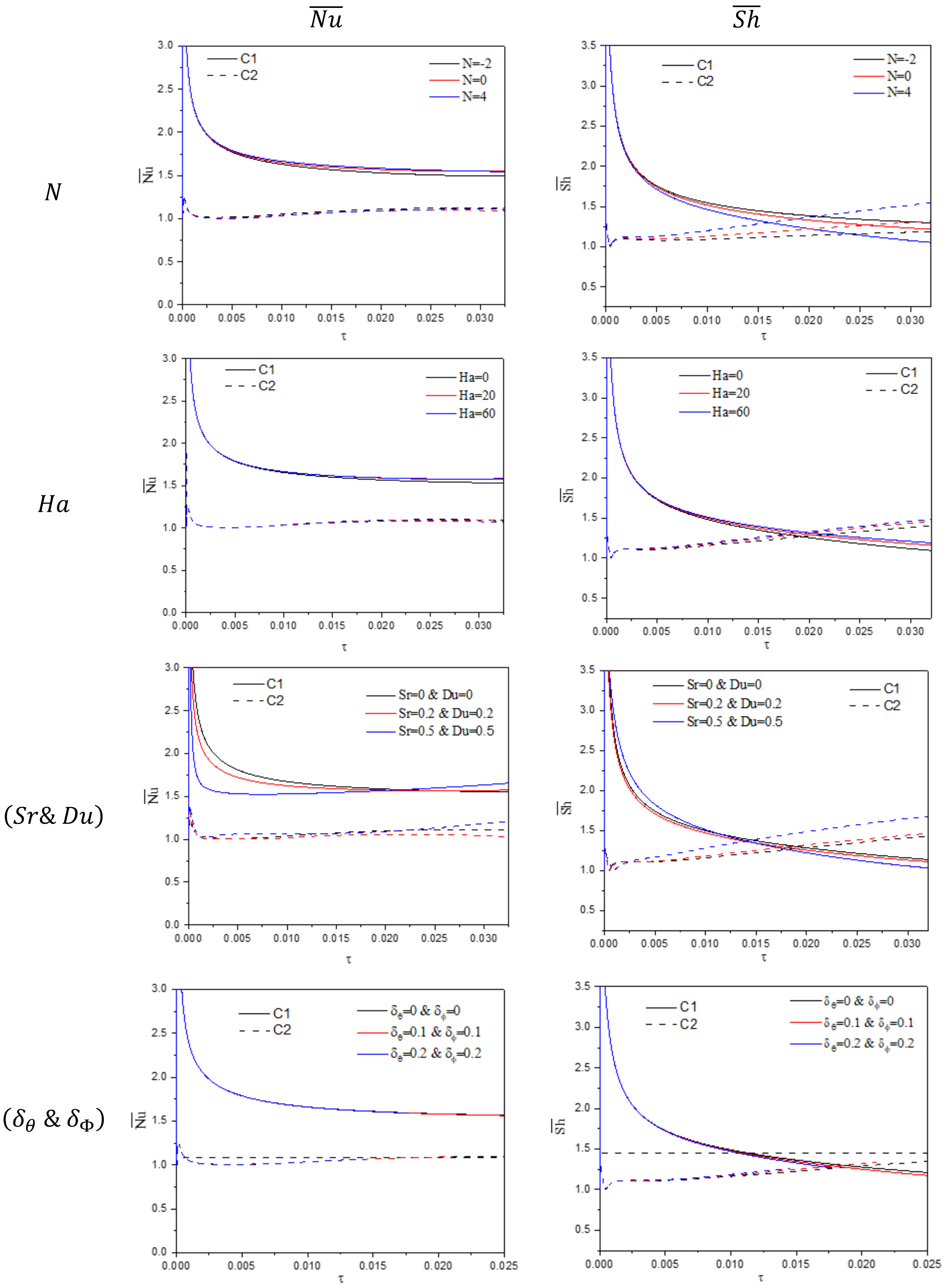

Figure 20. Average $\overline{Nu}$ and $\overline{Sh}$ under the variations of N, Ha, $(Sr\& \, Du)$, and $(\delta_\theta \ \& \ \delta_\Phi)$ at C1 and C2.

6. Conclusions

The ANN model is used in conjunction with the ISPH simulation to manage Ca-Ch heat and NEPCM mass transport within a curvilinear cavity during an exothermic process. Two cases of boundary conditions for curvilinear cavities are conducted in this work. ANN model forecasts the values of $\overline{Nu}$ and $\overline{Sh}$ based on the ISPH simulations. We investigated the transfer of heat and mass under the numbers of Frank-Kamenetskii, Hartmann, Rayleigh, Soret, and Dufour and the buoyancy ratio parameter. Our major conclusions are as follows:

- The ANN model predicted the values of $\overline{Nu}$ and $\overline{Sh}$ based on the target values of ISPH simulation.
- Two boundary conditions for a curvilinear cavity have a significant impact on enhancing mass, heat transfer, heat capacity ratio, and velocity field within a cavity.
- The Ca–Ch heat and mass transfer parameters effectively reduce the temperature and concentration inside a curvilinear cavity at C1 and C2. The velocity field decreases by 44.1% and 48.9% at C1 and C2, respectively when δ_θ & δ_Φ are increased from 0 to 0.2.
- An increase in the Power law index n from 1.1 to 1.4, declines the velocity field by 64.68% and 64.66% at C1 and C2, respectively.
- Increasing Soret and Dufour numbers $(Sr \,\&\, Du)$ supports the distribution of concentration. When Sr and Du are increased from 0 to 0.5, the velocity field increases by 34.17% and 29.73%, respectively at C1 and C2.

Author contributions

Weaam Alhejaili and Abdelraheem M. Aly were responsible for the conceptualization, methodology, validation, and supervision of the study, with Weaam Alhejaili leading the writing of the original draft and Abdelraheem M. Aly reviewing and editing; Munirah Alotaibi contributed to data curation, software implementation, visualization, and formal analysis, while all authors participated in project administration and approved the final version of the manuscript.

Use of Generative-AI tools declaration

The authors declare they have not used Artificial Intelligence (AI) tools in the creation of this article.

Acknowledgments

The authors extend their appreciation to the Deanship of Scientific Research at King Khalid University, Abha, Saudi Arabia, under Grant Number (RGP. 2/610/45). The authors extend their appreciation to the Deanship of Scientific Research and Libraries in Princess Nourah bint Abdulrahman University for funding this research work through the Research Group project, Grant No. (RG-1445-0001). The authors thank Aishah Alshehri for her contributions as an assistant researcher for this paper.

Conflict of interest

All authors declare that they have no conflicts of interest. The authors declare that they have no known competing financial interests or personal relationships that could have appeared to influence the work reported in this paper.

References

1. W. S. McCulloch, W. Pitts, A logical calculus of the ideas immanent in nervous activity, *Bull. Math. Biophys.*, **5** (1943), 115−133. https://doi.org/10.1007/BF02478259
2. N. Metropolis, A. W. Rosenbluth, M. N. Rosenbluth, A. H. Teller, E. Teller, Equation of state calculations by fast computing machines, *J. Chem. Phys.*, **21** (1953), 1087−1092. https://doi.org/10.1063/1.1699114
3. D. E. Rumelhart, G. E. Hinton, R. J. Williams, Learning representations by back-propagating errors, *Nature*, **323** (1986), 533−536. https://doi.org/10.1038/323533a0
4. I. E. Lagaris, A. Likas, D. I. Fotiadis, Artificial neural networks for solving ordinary and partial differential equations, *IEEE T. Neur. Net.*, **9** (1998), 987−1000. https://doi.org/10.1109/72.712178
5. A. Shafiq, A. B. Çolak, T. N. Sindhu, Designing artificial neural network of nanoparticle diameter and solid-fluid interfacial layer on single-walled carbon nanotubes/ethylene glycol nanofluid flow on thin slendering needles, *Int. J. Numer. Meth. Fl.*, **93** (2021), 3384−3404. https://doi.org/10.1002/fld.5038
6. S. K. Mitusch, S. W. Funke, M. Kuchta, Hybrid FEM-NN models: Combining artificial neural networks with the finite element method, *J. Comput. Phys.*, **446** (2021), 110651. https://doi.org/10.1016/j.jcp.2021.110651
7. K. U. Rehman, A. B. Çolak, W. Shatanawi, Artificial neural networking (ANN) model for drag coefficient optimization for various obstacles, *Mathematics*, **10** (2022). https://doi.org/10.3390/math10142450
8. M. Sahu, S. Jana, S. Agarwal, K. K. Khatua, S. Mohapatra, *Point form velocity prediction in meandering open channel using artificial neural network*, In: 2nd International Conference on Environmental Science and Technology, 6, IACSIT Press, Singapore, 2011.
9. A. M. Aly, S. W. Lee, H. S. Hussein, Integrating ISPH simulations with machine learning for thermal radiation and exothermic chemical reaction on heat and mass transfer in spline/triangle star annulus, *Case Stud. Therm. Eng.*, **54** (2024), 103948. https://doi.org/10.1016/j.csite.2023.103948
10. A. Gholami, H. Bonakdari, S. A. Fenjan, A. A. Akhtari, Flow variables prediction using experimental, computational fluid dynamic and artificial neural network models in a sharp bend, *Int. J. Eng.*, **29** (2016), 14−22. https://doi.org/10.5829/idosi.ije.2016.29.01a.03
11. C. Rackauckas, Y. Ma, J. Martensen, C. Warner, K. Zubov, R. Supekar, et al., Universal differential equations for scientific machine learning, *arXiv preprint*, 2020. https://doi.org/10.48550/arXiv.2001.04385
12. S. Motahar, A neural network approach to estimate non-Newtonian behavior of nanofluid phase change material containing mesoporous silica particles, *Int. J. Eng.*, **34** (2021), 1974−1981. https://doi.org/10.5829/ije.2021.34.08b.18
13. M. Ramezanizadeh, M. H. Ahmadi, M. A. Nazari, M. Sadeghzadeh, L. Chen, A review on the utilized machine learning approaches for modeling the dynamic viscosity of nanofluids, *Renew. Sust. Energ. Rev.*, **114** (2019), 109345. https://doi.org/10.1016/j.rser.2019.109345

14. A. Ali, S. U. Ilyas, S. Garg, M. Alsaady, K. Maqsood, R. Nasir, et al., Dynamic viscosity of Titania nanotubes dispersions in ethylene glycol/water-based nanofluids: Experimental evaluation and predictions from empirical correlation and artificial neural network, *Int. Commun. Heat Mass*, **118** (2020), 104882. https://doi.org/10.1016/j.icheatmasstransfer.2020.104882
15. M. H. Ahmadi, M. Sadeghzadeh, H. Maddah, A. Solouk, R. Kumar, K. Chau, Precise smart model for estimating dynamic viscosity of SiO_2/ethylene glycol-water nanofluid, *Eng. Appl. Comput. Fluid Mech.*, **13** (2019), 1095−1105. https://doi.org/10.1080/19942060.2019.1668303
16. R. A. Gingold, J. J. Monaghan, Smoothed particle hydrodynamics: Theory and application to non-spherical stars, *Mon. Not. R. Astron. Soc.*, **181** (1977), 375−389. https://doi.org/10.1093/mnras/181.3.375
17. A. Ferrari, SPH simulation of free surface flow over a sharp-crested weir, *Adv. Water Resour.*, **33** (2010), 270−276. https://doi.org/10.1016/j.advwatres.2009.12.005
18. M. Hopp-Hirschler, M. S. Shadloo, U. Nieken, A smoothed particle hydrodynamics approach for thermo-capillary flows, *Comput. Fluid.*, **176** (2018), 1−19. https://doi.org/10.1016/j.compfluid.2018.09.010
19. M. S. Shadloo, G. Oger, D. Le Touzé, Smoothed particle hydrodynamics method for fluid flows, towards industrial applications: Motivations, current state, and challenges, *Comput. Fluid.*, **136** (2016), 11−34. https://doi.org/10.1016/j.compfluid.2016.05.029
20. Z. T. Yu, X. Xu, Y. C. Hu, L. W. Fan, K. F. Cen, A numerical investigation of transient natural convection heat transfer of aqueous nanofluids in a horizontal concentric annulus, *Int. J. Heat Mass*, **55** (2012), 1141−1148. https://doi.org/10.1016/j.ijheatmasstransfer.2011.09.058
21. A. Yılmazer, C. Kocar, A novel analytical method for heat conduction in convectively cooled eccentric cylindrical annuli, *Int. J. Therm. Sc.*, **83** (2014), 1−15. https://doi.org/10.1016/j.ijthermalsci.2014.04.008
22. R. W. Lewis, K. Morgan, H. Thomas, *The finite element method in heat transfer analysis*, John Wiley & Sons, 1996.
23. R. W. Lewis, R. W. Lewis, B. Schrefler, *The finite element method in the static and dynamic deformation and consolidation of porous media*, John Wiley & Sons, 1998.
24. M. Ghalambaz, A. J. Chamkha, D. Wen, Natural convective flow and heat transfer of Nano-Encapsulated Phase Change Materials (NEPCMs) in a cavity, *Int. J. Heat Mass*, **138** (2019), 738−749. https://doi.org/10.1016/j.ijheatmasstransfer.2019.04.037
25. S. M. H. Zadeh, S. A. M. Mehryan, M. Sheremet, M. Ghodrat, M. Ghalambaz, Thermo-hydrodynamic and entropy generation analysis of a dilute aqueous suspension enhanced with nano-encapsulated phase change material, *Int. J. Mech. Sci.*, **178** (2020), 105609. https://doi.org/10.1016/j.ijmecsci.2020.105609
26. M. Ghalambaz, S. A. M. Mehryan, N. Mashoofi, A. Hajjar, A. J. Chamkha, M. Sheremet, et al., Free convective melting-solidification heat transfer of nano-encapsulated phase change particles suspensions inside a coaxial pipe, *Adv. Powder Technol.*, **31** (2020), 4470−4481. https://doi.org/10.1016/j.apt.2020.09.022
27. C. J. Ho, Y. C. Liu, T. F. Yang, M. Ghalambaz, W. M. Yan, Convective heat transfer of nano-encapsulated phase change material suspension in a divergent minichannel heatsink, *Int. J. Heat Mass*, **165** (2021), 120717. https://doi.org/10.1016/j.ijheatmasstransfer.2020.120717
28. Z. Raizah, A. M. Aly, Double-diffusive convection of a rotating circular cylinder in a porous cavity suspended by nano-encapsulated phase change materials, *Case Stud. Therm. Eng.*, **24** (2021), 100864. https://doi.org/10.1016/j.csite.2021.100864

29. A. M. Aly, Z. Raizah, A. Al-Hanaya, Double rotations between an inner wavy shape and a hexagonal-shaped cavity suspended by NEPCM using a time-fractional derivative of the ISPH method, *Int. Commun. Heat Mass*, **127** (2021), 105533. https://doi.org/10.1016/j.icheatmasstransfer.2021.105533
30. S. R. Afshar, S. R. Mishra, A. S. Dogonchi, N. Karimi, A. J. Chamkha, H. Abulkhair, Dissection of entropy production for the free convection of NEPCMs-filled porous wavy enclosure subject to volumetric heat source/sink, *J. Taiwan Inst. Chem. E.*, **128** (2021), 98−113. https://doi.org/10.1016/j.jtice.2021.09.006
31. B. Zalba, J. M. Marín, L. F. Cabeza, H. Mehling, Review on thermal energy storage with phase change: Materials, heat transfer analysis and applications, *Appl. Therm. Eng.*, **23** (2003), 251−283. https://doi.org/10.1016/S1359-4311(02)00192-8
32. L. F. Cabeza, A. Castell, C. Barreneche, A. De Gracia, A. I. Fernández, Materials used as PCM in thermal energy storage in buildings: A review, *Renew. Sust. Energ. Rev.*, **15** (2011), 1675−1695. https://doi.org/10.1016/j.rser.2010.11.018
33. P. K. S. Rathore, S. K. Shukla, Potential of macroencapsulated PCM for thermal energy storage in buildings: A comprehensive review, *Constr. Build. Mater.*, **225** (2019), 723−744. https://doi.org/10.1016/j.conbuildmat.2019.07.221
34. J. Giro-Paloma, M. Martínez, L. F. Cabeza, A. I. Fernández, Types, methods, techniques, and applications for microencapsulated phase change materials (MPCM): A review, *Renew. Sust. Energ. Rev.*, **53** (2016), 1059−1075. https://doi.org/10.1016/j.rser.2015.09.040
35. A. M. Aly, Z. Raizah, S. El-Sapa, H. F. Oztop, N. Abu-Hamdeh, Thermal diffusion upon magnetic field convection of nano-enhanced phase change materials in a permeable wavy cavity with crescent-shaped partitions, *Case Stud. Therm. Eng.*, **31** (2022), 101855. https://doi.org/10.1016/j.csite.2022.101855
36. G. R. Kefayati, Simulation of heat transfer and entropy generation of MHD natural convection of non-Newtonian nanofluid in an enclosure, *Int. J. Heat Mass Tran.*, **92** (2016), 1066−1089. https://doi.org/10.1016/j.ijheatmasstransfer.2015.09.078
37. S. Acharya, S. K. Dash, Natural convection in a cavity with undulated walls filled with water-based non-Newtonian power-law CuO-water nanofluid under the influence of the external magnetic field, *Numer. Heat Tr. A-Appl.*, **76** (2019), 552−575. https://doi.org/10.1080/10407782.2019.1644898
38. J. Bonet, S. Kulasegaram, Correction and stabilization of smooth particle hydrodynamics methods with applications in metal forming simulations, *Int. J. Numer. Meth. Eng.*, **47** (2000), 1189–1214. https://doi.org/10.1002/(SICI)1097-0207(20000228)47:6%3C1189::AID-NME830%3E3.0.CO;2-I
39. M. Paroncini, F. Corvaro, Natural convection in a square enclosure with a hot source, *Int. J. Therm. Sci.*, **48** (2009), 1683−1695. https://doi.org/10.1016/j.ijthermalsci.2009.02.005
40. L. Hardesty, Explained: neural networks, *MIT News*, **14** (2017).
41. A. Brahme, *Comprehensive biomedical physics*, Elsevier, 2014.
42. A. B. Çolak, A new study on the prediction of the effects of road gradient and coolant flow on electric vehicle battery power electronics components using machine learning approach, *J. Energy Storage*, **70** (2023), 108101. https://doi.org/10.1016/j.est.2023.108101

AIMS Press

© 2024 the Author(s), licensee AIMS Press. This is an open access article distributed under the terms of the Creative Commons Attribution License (http://creativecommons.org/licenses/by/4.0)